Towards High Temperature Light-Induced Spin State Trapping in Spin Crossover materials: the Interplay of Collective and Molecular Effects

M. Nadeem,[†] Jace Cruddas,[‡] Gian Ruzzi,[†] and Ben J. Powell[*,†]

†*School of Mathematics and Physics, The University of Queensland, Brisbane, Queensland, 4072, Australia*

‡*School of Physical Sciences, The University of Adelaide, SA 5005, Australia*

E-mail: powell@physics.uq.edu.au

Abstract

Spin crossover (SCO) materials display many fascinating behaviors including collective phase transitions and spin-state switching controlled by external stimuli, e.g., light and electrical currents. As single molecule switches, they have been fêted for numerous practical applications, but these remain largely unrealized – partly because of the difficulty of switching these materials at high temperatures. Here we introduce a semi-empirical microscopic model of SCO materials combining crystal field theory with elastic intermolecular interactions. We show that, for realistic parameters, this model reproduces the key experimental results including thermally induced phase transitions, light-induced spin-state trapping (LIESST), and reverse-LIESST. Notably, our model reproduces and explains the experimentally observed relationship between the critical temperature of the thermal transition, $T_{1/2}$, and the highest temperature for which the trapped state is stable, T_{LIESST}. We propose strategies to design SCO materials with higher T_{LIESST}: increasing the stiffness of the coordination sphere, optimizing the

spin-orbit coupling via heavier atoms (particularly in the inner coordination sphere), and minimizing the enthalpy difference between the high-spin (HS) and low-spin (LS) states can all increase T_{LIESST}. However, the most dramatic increases arise from increasing the cooperativity of the spin-state transition by increasing the rigidity of the crystal. Increased crystal rigidity can also stabilize the HS state to low temperatures on thermal cycling, yet leave the LS state stable at high temperatures following, for example, reverse-LIESST. We show that such highly cooperative systems offer a realistic route to robust room temperature switching, demonstrate this *in silico*, and discuss material design rationale to realize this experimentally.

Introduction

Switching is central to modern computer logic, displays and memory. Thus, the quest for greater miniaturization and efficiency often focuses on switches, e.g., transistors. The majority of the world's data is currently stored in 600 hyperscale data centers, which each consume hundreds of megawatts of electricity annually.[1] So developing smaller, more efficient, switches is an environmental, as well as a technological, priority.

Several molecular switches have been explored including single molecule magnets,[2] valance tautomerism,[3] electron transfer coupled spin transitions[4] (in, e.g., Prussian blue analogues,[5] molecular systems,[6] and coordination polymers[7]), and spin crossover (SCO) materials.[8] SCO complexes display two spin-states; and are intrinsically multifunctional as changes in spin-state simultaneously lead to changes in electronic and magnetic properties, size and color. This has led to proposed applications[8–10] of SCO materials as sensors,[11,12] displays,[13,14] high-density memory,[14,15] molecular electronics,[16] spintronics,[17,18] mechanical actuators,[19,20] intelligent contrast agents for magnetic resonance imaging,[21] and nanophotonics.[10,22]

For molecules in solution varying the temperature leads to a crossover: at high temperatures most molecules are high spin (HS), but at low temperatures most are low spin (LS).[8] The crossover is characterized by the temperature ($T_{1/2}$) at which half the molecules are HS

and half are LS. $T_{1/2}$ is determined by the ratio of the enthalpy (ΔH) and entropy (ΔS) differences between the HS and LS states: $T_{1/2} = \Delta H/\Delta S$. However, in crystalline materials (including nanocrystals) elastic interactions between molecules can be strong enough for this crossover to become a thermodynamic phase transition, whereby almost all molecules are HS for $T > T_{1/2}$ and almost all are LS for $T < T_{1/2}$.

A particularly attractive feature of SCO materials is that they display excited spin state trapping. Here an external stimuli is used to switch between the two spin-states. At low temperatures the excited spin-state is 'trapped', i.e., is a long lived metastable state. Most prominently, the excited spin state can be populated via light irradiation, which is known as light-induced excited spin state trapping (LIESST)[23,24] and depopulated by irradiation at a different wavelength, referred to as reverse-LIESST.[24] There are also several of materials that remain HS at all temperatures on cooling, but where a LS phase can be induced by a reverse-LIESST process and the LS state then remains stable (without further irradiation) to some high temperature.[25–28]

The pathways by which light populates and depopulates the excited spin states, and the reverse process, have been mapped in considerable detail, both experimentally[23,29–40] and theoretically.[41–43] Therefore, we will not discuss these mechanisms in detail below. Instead, we focus on the observation that above some temperature the excited state decays rapidly. This temperature is denoted T_{LIESST} for HS decaying to LS and $T_{\mathrm{r\text{–}LIESST}}$ for LS decaying to HS. A major goal of the field is to increase the temperature range where SCO materials can be switched by an external stimuli, ideally to a wide temperature range around room temperature, which would be an important step towards practical applications of SCO materials.[9]

Our primary goal here is to facilitate progress towards high temperature bistability by providing a detailed microscopic theory of the collective dynamics of crystalline materials following excited spin-state trapping. To do so we introduce a unified theory of the photo- and thermally-induced properties of spin-crossover materials. This requires a model that

captures both the quantum mechanical intramolecular transitions and the classical intermolecular elastic interactions. We achieve this by combining crystal field theory with elastic models of intra- and inter-molecular vibrations. This allows us to propose specific new strategies to design SCO complexes with higher T_{LIESST} or $T_{\mathrm{r\text{–}LIESST}}$. These include increasing the stiffness of the inner coordination sphere, increasing the rigidity of the lattice to enhance cooperative effects that stabilize excited spin states, increasing the effective spin-orbit coupling via heavier atoms (particularly in the inner coordination sphere), and minimizing the enthalpy difference between the HS and LS states. However, we emphasize that the goal is bistable switching at high temperatures and not high T_{LIESST} per se – we show, theoretically, that systems that remain HS to low temperatures but allow reverse-LIESST offer a realistic possibility of achieving this and demonstrate room temperature bistability *in silico*.

The HS–LS transition is spin forbidden; but allowed by spin-orbit coupling, which is weak. Buhks *et al.*[44] exploited the weakness of spin-orbit coupling to calculate the temperature-dependent radiationless HS→LS rate, $k_{HL}(T)$, for molecules in solution from perturbation theory, which agrees well with experimental data. In the high-temperature limit this theory predicts that the rate is thermally activated. However, as $T \to 0$ the rate goes to a constant value due to quantum nuclear tunneling. Hauser[45–47] used Buhks *et al.*'s methodology to argue that the low temperature HS→LS rate depends strongly on the energy gap between the HS and LS state, ΔH; specifically $k_{HL}(T \to 0) \propto e^{\Delta H/\hbar\omega}$, where ω is the typical frequency of molecular vibrations. Thus, Hauser proposed that $\ln[k_{HL}(T \to 0)] \propto T_{1/2}$ and showed that this 'inverse energy gap law' is in good agreement with experimental data.[45,48]

A variety of methods have been explored to enable excited spin-state trapping in SCO materials. With an eye to potential technologies it is important that the spin state can be switched by a electrical current (electron-induced spin state trapping; EIESST) and in a single molecule.[49–55] Other methods of creating excited spin states include thermal-quenching induced excited spin state trapping (TIESST),[56–58] nuclear-decay induced excited spin state trapping (NIESST),[59] hard x-ray induced excited spin state trapping (HAXIESST).[60] But

LIESST remains, by far, the most studied method.

Light-induced switching has also been observed in the thermal hysteresis loop.[61] A challenge that needs to be overcome to enable practical applications of switching in this regime is that a wide hysteresis loop (in the slow cycling limit) near room temperature are required. Therefore, an important goal is to understand how to increase the hysteresis width while maintaining the bistable region at room temperature.

A standard protocol has been established for LIESST experiments:[62] first a sample is cooled to the low temperature LS phase; it is then irradiated with a single frequency of light at 10 K until it reaches an HS phase; the irradiation is then discontinued and the sample is heated at the rate of 0.3 K/minute. This standardization has facilitated the identification of several important correlations with other properties of SCO materials and structure-property relationships.[62,63] The most prominent relationship is that, for many families of SCO materials with the same inner coordination sphere and ligands with the same denticity, $T_{\mathrm{LIESST}} = T_0 - aT_{1/2}$, where T_0 and a are constants.[24,48] Thus, T_0 sets an upper limit for T_{LIESST} within a given family of materials. A strong variation of T_0 is observed with the denticity of the ligands,[64] with higher denticity leading to higher T_0, and thus higher T_{LIESST}. It was initially proposed[24,48,65] that $a \simeq 0.3$ in all families. But, recent work has shown that a varies significantly between families of SCO materials.[24,66]

The inverse correlation between T_{LIESST} and $T_{1/2}$ is often discussed in terms of Hauser's inverse energy gap law. But, there is an important subtly here, which is frequently neglected. Hauser's result concerns the quantum tunneling HS→LS rate, and therefore is only relevant in the low temperature limit ($T \to 0$). On the other hand T_{LIESST} can be relatively large ($T_{\mathrm{LIESST}} > 130$ K has been reported[67]) and thus well into the classical thermally activated regime. Therefore, quantum nuclear tunneling and the inverse energy gap law do not provide a full explanation of the inverse correlation between T_{LIESST} and $T_{1/2}$.

Several lines of experimental evidence indicate that interactions between SCO centers have significant effects on the behaviors of trapped excited spin-states.[27,63,66,68] It has been

shown that interactions can modify the relationship between T_{LIESST} and $T_{1/2}$, changing both a and T_0.[66] Metal dilution experiments provide an elegant way to probe the effects of interactions as in highly dilute mixed crystals collective effects are weak or absent.[27,63] For example, experiments on $\{[Zn_{1-x}Fe_x(bbtr)_3](BF_4)_2\}_\infty$ have shown that interactions increase T_{LIESST} and can drive the photo-excited system into a different thermodynamic phase.[27] Therefore, a proper understanding of the correlations of T_{LIESST} with $T_{1/2}$ requires a theory, like that presented below, that can describe both intramolecular transitions and collective properties at the same time.

An important approach to understanding T_{LIESST} has been studying macroscopic models with temperature dependent rate constants via the master equation formalism.[48] This approach allows cooperativity between multiple SCO molecules to be included, although this is limited to a mean-field treatment.[48,68] These models suggest that cooperativity results in a faster decay of the light-induced HS state. However, metal dilution experiments show that interactions lead to relaxation dynamics that are not described correctly by these macroscopic theories.[27,63] Nevertheless, a clear conclusion from this body of experimental and theoretical work is that the thermally activated processes are crucial in determining T_{LIESST}.

An alternative approach to understanding collective effects is to study phenomenological 'Ising-like' models.[69,70] These models have been shown to reproduce most of the important conclusions drawn from macroscopic rate constant models, particularly in the thermally activated decay regime.[71–73] Ising-like models have also been shown to describe multistep transitions that are observed in some SCO materials and have been used to predict exotic new phases of these materials.[18,70,74–77] In principle, this approach also allows one to study correlation effects beyond mean field; however, to date, most studies are in the mean field approximation.[71–73] A serious limitation of Ising-like models is that they contain many phenomenological parameters; and the connection of many of these phenomenological parameters to the underlying physics and chemistry of materials remains obscure.

Model

In this section, we briefly describe our macroscopic model and its derivation from crystal field theory, the full mathematical derivation is given in the supplementary information, as is a discussion of the parameters values relevant to SCO materials (typical parameter ranges are summarized in table 1). We use crystal field theory to provide a microscopic foundation for our model as this is the simplest theory that describes spin crossover in coordination complexes. As many of the parameters in crystal field theory for specific materials and, more importantly, the trends which parameters follow across chemical series are known this allows us to make specific predictions of how to chemically engineer behaviors of new SCO materials on the basis of this model.[78,79] The most dramatic structural change on SCO is the metal-ligand bond length. Therefore, we include this mode explicitly in the ligand field theory. Spin orbit coupling is also included as without this effect the SCO transition is spin forbidden. Finally, we include the elastic coupling between SCO centers, which is known to be vital for understanding collective effects in the solid state.[18,69,70,70–77]

Table 1: Realistic values of the parameters in our model. We give both the range found in typical SCO materials and a "default" value in the center of this range that will be used in many of the calculations below. Detailed discussion of the parameters values is given in the supplementary information.

Parameter	**Range**	**Refs**	**Default value**
B	90–105 meV	[44,80]	100 meV
C/B	4.41	[78]	4.41
Dq/B	2.034–2.106	[78]	2.05
ζ	2–40 meV	[81–83]	15 meV
k	5–15 eV/Å^2	[84,85]	10 eV/Å^2
κ	0.75-5.5 eV/Å^2	[86,87]	0.75 eV/Å^2
δ	0.08-0.15 Å	[87,88]	0.11 Å
ω_{HS}	100–500 cm^{-1}	[87]	220 cm^{-1}
ω_{LS}	100–500 cm^{-1}	[87]	300 cm^{-1}
k_1	0–20 eV/Å^2	[89,90]	1.5 eV/Å^2
k_2	0–20 eV/Å^2	[76,89,90]	65 meV/Å^2

Given the standard assumption[78] that the ratio of Racah parameters is fixed, $C/B \simeq 4.41$,

the crystal field theory of d^6 octahedral complexes is specified by the ratio of the crystal field splitting, Dq, to the Racah parameter, B, which parameterizes the effective Coulomb interaction between electrons. This insight enables the drawing of Tanabe-Sugano diagrams. We include only the three lowest energy terms in our model: *vis.* the low spin (LS; $^1A_1$) , intermediate spin (IS; $^3T_1$), and high-spin (HS; $^5T_2$) states.

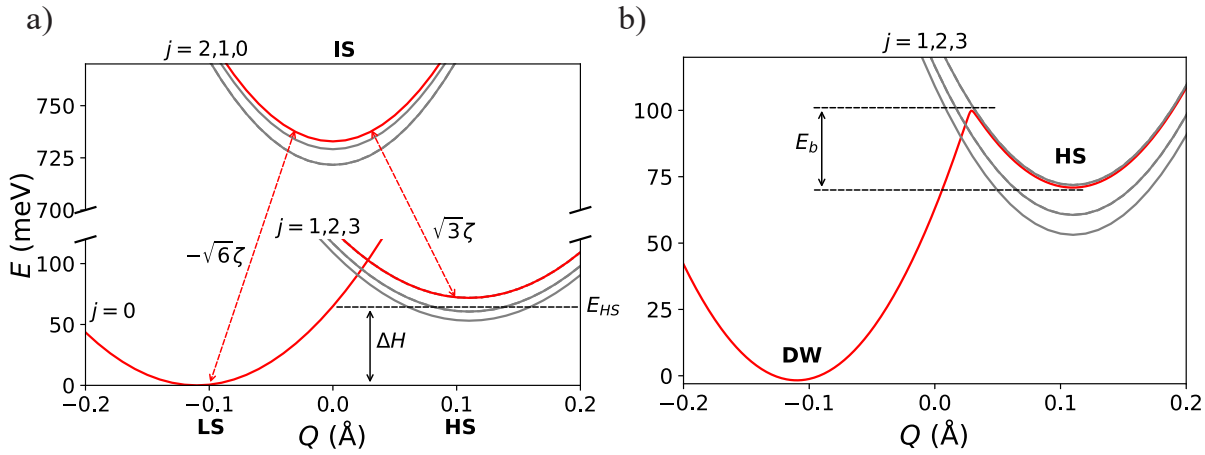

Figure 1: Crystal field theory of a d^6 SCO metal-center in an octahedral ligand-potential, at $T = 0$ K. (a) Potential energy surfaces of the three low energy terms – $^1A_1$ (LS), $^3T_1$ (IS) and $^5T_2$ (HS). Q is the difference of the metal-ligand bond length from the minimum energy bond length in the IS state. E_{HS} is energy of the HS state neglecting spin-orbit coupling and ΔH is the enthalpy difference between LS and HS states. The spin-orbit coupling splits the states with different total angular momentum j. The dashed arrows mark the spin-orbit couplings between the trivial irreducible representation (red curves) of the octahedral double-group. Spin-orbit coupling between non-trivial irreducible representations are not implicated in SCO. (b) Potential energy surfaces after integrating out the high energy intermediate spin level. The double well (DW; red) state is a mixture of the trivial states of the LS, IS and HS terms, whereas the non-trivial HS states (gray) are not mixed. E_b is the classical energy barrier in a single spin-crossover molecule. In both plots we use the default parameters given in table 1.

We explicitly include the symmetric breathing metal-ligand stretching mode which we assume is classical and harmonic, with a spring constant that depends on the spin state with $k_{\mathrm{LS}} = k + \kappa$, $k_{\mathrm{IS}} = k$, and $k_{\mathrm{HS}} = k - \kappa$, as the higher spin states have a greater occupation of e_g^* orbitals. The occupation of antibonding orbitals also increases the metal-ligand bond length. To account for this we measure the bond length, Q, relative to the minimum energy length in the IS state, and set the minimum energy bond length to be $Q = -\delta$ in the LS

state and $Q = \delta$ in the HS state, figure 1a. The remaining vibrational modes are only included implicitly via their contribution to the entropy difference, ΔS, between the HS and LS states, which we model by assuming that all asymmetric modes take the same 'average' frequency, which takes different values in the HS (ω_{HS}) and LS states (ω_{LS}). We also assume that these asymmetric vibrations allow (barrierless) transitions within the HS states, some of which are otherwise forbidden.

Spin-orbit coupling, ζ, introduces zero-field splitting among the IS and HS terms and allows the intersystem crossings LS⇆IS and IS⇆HS, figure 1a. We integrate out the IS level via a canonical transformation.[91–93] This leaves an effective low-energy model consisting of a double well (DW) potential that has mixed HS/IS/LS character and fourteen pure HS states, figure 1b.

We place the SCO molecules on a square lattice and assume elastic interactions between the ligands in neighboring molecules. We set the spring constants to k_1 for nearest neighbors, k_2 for next nearest neighbors, and neglect longer range interactions, scheme 1.

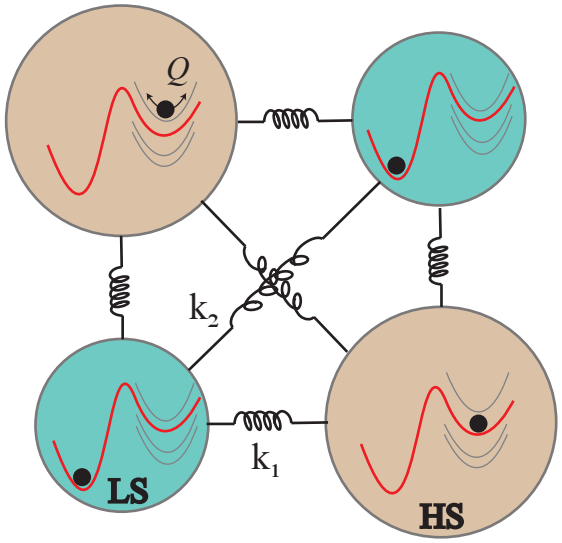

Scheme 1: The square lattice with nearest neighbor (k_1) and next nearest neighbor (k_2) elastic interactions and internal potential surfaces, as detailed in figure 1.

Methods

The model introduced above describes a system of interacting classical oscillators with multiple internal potentials. We use classical molecular dynamics to simulate the dynamic evolution of the system with probabilistic hops between the potential energy surfaces describing individual molecules governed by classical Monte Carlo. After the system evolves for 50 molecular dynamics steps, we apply 20 Monte-Carlo steps on each site to set the thermal distribution of the internal potentials. Here we study a two-dimensional system on a square lattice 30×30 with periodic boundary conditions. Additional details of the simulation scheme are given in the supplementary information.

Molecular Dynamics

We use the Nose-Hoover thermostat and the Anderson barostat.[94] To ensure equipartition, we use massive thermostating for positions and internal coordinates.[95] The equations of motion, which are given in the supplementary information, were integrated using the multistep predictor-corrector method.[96]

Monte-Carlo

At a configuration given by the set $\{Q_i, \boldsymbol{r}_i, \nu_i\}$, we use the Metropolis criteria to allow transitions between the internal HS potential energy surfaces. Since the double well state, $|\mathrm{DW}\rangle$, mixes LS, IS, and HS states, a transition from the DW potential to the other HS levels is allowed only if $|\left\langle \mathrm{HS}, 3, \overline{A}_1, 0 \middle| \mathrm{DW} \right\rangle|^2 \geq \rho$, where ρ is a random number uniformly chosen from the interval $[0, 1]$ and $\left|\mathrm{HS}, 3, \overline{A}_1, 0\right\rangle$ is the trivial representation of the HS state.

Results and Discussion

To simulate cooling from high temperatures we initialized the system in the all HS state and then equilibrated at 300 K before lowering the temperature from 300 K to 10 K in steps of 2 K. To simulate the LIESST, EIESST, TIESST, NIESST, and HAXIESST experiments we initialized the system in the all HS state and then equilibrated at 10 K before raising the temperature from 10 K to 300 K in steps of 2 K. This protocol does not attempt to model the optical[23,29–43] (LIESST), electronic (EIESST), non-equilibrium (TIESST), nuclear (NIESST), or x-ray (HAXIESST) driven excitation pathways that cause the population excited high spin molecules, but aims to describe the trapping of the excited spin-states and the collective dynamics of the system after the population is created, e.g., once the light or current is switched off, or the quench is completed. Thus, for simplicity, we will discuss our results below in terms of light induced changes in spin-state; but we emphasize that our results are equally applicable to changes in spin-state due to the systems response to other stimuli.

Representative plots of the magnetic susceptibilities calculated following this protocol are shown in figure 2. All data sets show spin-state trapping at low temperatures (for $T < T_{\mathrm{LIESST}}$) and a thermally induced change in the stable state (the LS state is stable for $T < T_{1/2}$ and the HS state is stable for $T > T_{1/2}$). Two distinct behaviors are observed in the thermally induced transition: in the weak cooperativity regime (figure 2a) one observes a crossover (characterized by a continuous change in the χT and no hysteresis) from the HS to LS state as the temperature is lowered; as the cooperativity is increased (figure 2b; where we vary k_2, varying k_1 has a similar effect) the crossover is replaced by a first order spin-state transition (characterized by a discontinuous jump in χT and hysteresis). Further increasing cooperativity (figure 2c) increases the width of the hysteresis. When there is hysteresis the temperature at which half of the molecules are HS differs for heating, $T_{1/2\uparrow}$, and cooling, $T_{1/2\downarrow}$. In keeping with standard convention, we estimate the thermodynamic transition temperature as $T_{1/2} = (T_{1/2\uparrow} + T_{1/2\downarrow})/2$ in this case. More subtly, the model also

predicts a gentle decrease in χT at low-temperatures due to zero field splitting and that the low-temperature and high temperature susceptibilities of the HS state are not equal. Both of these observations are common experimentally, but are absent from many previous models of SCO materials. Thus, the model reproduces the key qualitative features of susceptibility measurements on SCO materials.

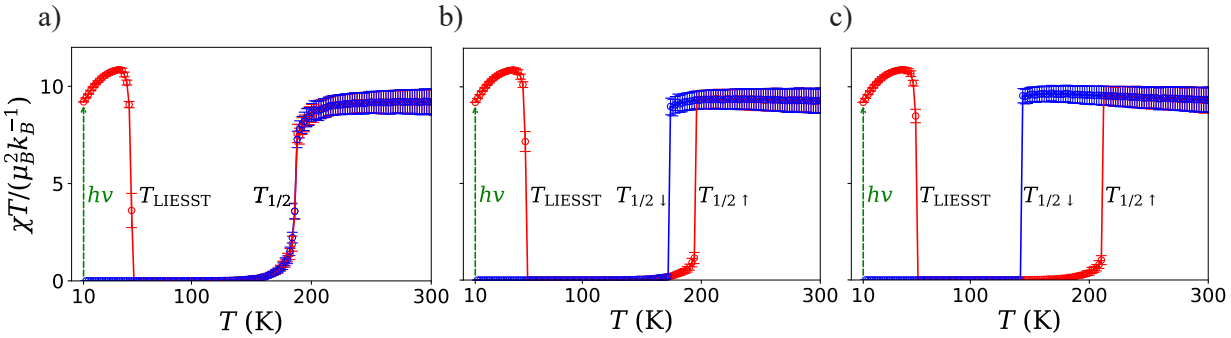

Figure 2: The calculated temperature dependence of the magnetic susceptibility displays a rich variety of collective behaviour observed in the LIESST experiments. The hysteresis increases with the interaction strength between the sites. (a) $k_2 = 65$ meV/Å^2, (b) $k_2 = 108$ meV/Å^2 and (c) $k_2 = 173$ meV/Å^2; all other parameters are set to the default values given in table 1. Simulations are shown for heating (red) and cooling (blue), both were initialized in an all HS state. The green arrow schematically indicates the light irradiation at 10 K in a LIESST experiment.

On varying the ligand field strength, Dq/B, we find an inverse correlation between the two temperatures that characterize SCO materials: $T_{\mathrm{LIESST}} = T_0 - aT_{1/2}$, where T_0 and a are constants, figure 3. This reproduces the trend observed experimentally.[24] It is interesting to note that our model has significantly less scatter than the experimental data.[24] This is presumably because our simple model allows us to independently vary one parameter at a time; whereas any chemical substitution necessarily changes multiple parameters simultaneously.

The inverse correlation between T_{LIESST} and $T_{1/2}$, figure 3, does *not* arise from Hauser's inverse energy gap law.[23,29,45] Our model entirely neglects that low temperature quantum nuclear tunneling that gives rise to the inverse energy gap law. Rather, the inverse correlation between T_{LIESST} and $T_{1/2}$ arises because T_{LIESST} is determined by the *classical* energy barrier between the HS and LS states in the DW potential. Increasing the ligand field splitting,

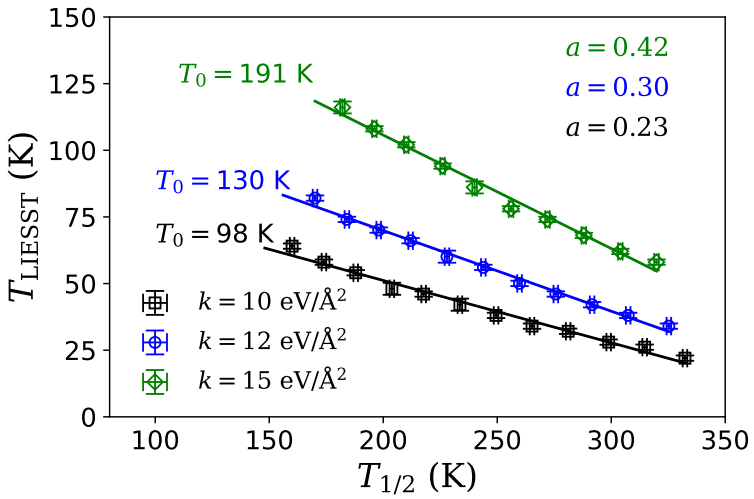

Figure 3: Predicted correlation between T_{LIESST} and $T_{1/2}$. Within each line, decreasing the ligand-field strength Dq decreases T_{LIESST} and increases $T_{1/2}$, i.e. $T_{\mathrm{LIESST}} = T_0 - aT_{1/2}$. Increasing the stiffness of the inner coordination sphere (k) increases T_0 and a; reminiscent of the experimentally observed variation between different families of SCO materials, where higher T_0 correlates with higher denticity of the ligand.[48] Thus we conclude that the primary effect of increased denticity is increasing the stiffness of the inner coordination sphere. For these simulations, we use $Dq/B = 2.022 - 2.078$ and rest of the parameters take their default values given in table 1.

Dq, simultaneously decreases E_b and increases ΔH, figure S3. A molecule trapped in the HS state needs enough thermal energy to cross the barrier in order to decay to the LS state. This analysis is supported by examining the dependence of T_{LIESST} and $T_{1/2}$ on the ligand field strength individually, figure 4. $T_{1/2}$ linearly increases with the ligand field strength, Dq/B. In contrast, T_{LIESST} linearly decreases with the ligand field strength.

Experimentally, T_0 is found to increase strongly with the denticity of the ligands.[24] Infrared spectroscopy shows that the frequency of the metal ligand breathing mode (ω_b) also increases with denticity (table S1). This is consistent with the intuitive notion that increasing the denticity of the ligand will increase the stiffness of breathing mode ($k \propto \omega_b^2$). On increasing the stiffness of the inner coordination sphere (k) we find that T_{LIESST} increases rapidly, but that $T_{1/2}$ does not change significantly (figures 4, S5, and **??**). This is consistent with the simple notion that the barrier between the HS and LS states, E_b, increases with k, (this is confirmed by explicit calculation, see figure S6). One expects that $T_{\mathrm{LIESST}} \propto E_b$ whereas

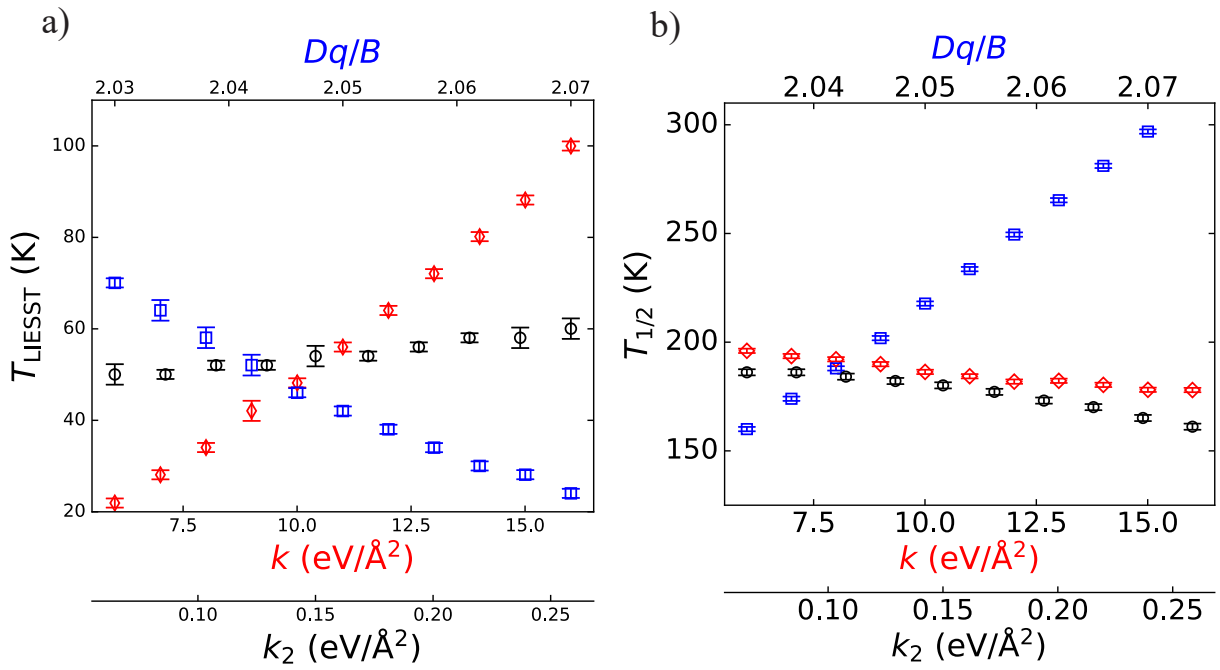

Figure 4: The effect of varying the key microscopic parameters on the (a) T_{LIESST} and (b) $T_{1/2}$. The color of the data points matches the label on the corresponding x-axis. T_{LIESST} varies strongly with the rigidity of the inner coordination sphere (k), the dimensionless ligand-field strength (Dq/B), and the elastic cooperatively due to k_2. Note that in these plots we are limited to very small values of k_2, cf. table 1. For larger k_2 we enter the region where $T_{\mathrm{LIESST}} > T_{1/2\uparrow}$; in this regime $T_{1/2}$ is not well defined and T_{LIESST} is effectively infinite [i.e., the HS state is (meta)stable at all temperatures]. In these plots all parameters except the one varied are set to the default values given in table 1.

$T_{1/2}$ is largely independent of E_b as the thermal transition occurs at higher temperatures.

Thus, our model predicts that increasing the stiffness of the inner coordination sphere leads to a pronounced increase in T_0, consistent with experiment (figure 3). We also find a small increase in a. This is difficult to compare with experiment because of the scatter in experimental data, the paucity of data for ligands with high denticity, and the subtly of the increase in a. However, a recent study focusing on a single family of complexes[66] has shown that the initial proposal that $a = 0.3$ is not universally correct and that a larger T_0 is correlated with a larger a. This is consistent with the clear prediction of our model that a increases with the stiffness of the inner coordination sphere and thus denticity. Note however, that for the parameters studied we find values of a close to 0.3 (figure 3).

As demonstrated above, we can qualitatively understand many of the behaviors of SCO materials in terms of the properties of individual molecules. However, the single molecule picture only describes our results semi-quantitatively as interactions between SCO centers cause significant changes to the predicted macroscopic behaviors in the solid state. Furthermore, understanding the role of these interactions is vital for designing new materials for potential applications of SCO materials. To more fully understand the role of the molecular environment we investigated the dependence of our model on the intermolecular elastic interactions, k_1 and k_2. T_{LIESST} is significantly enhanced by increased cooperativity, whereas $T_{1/2}$ is more weakly affected by varying the cooperative interaction strength, see figures 4 and S7. This demonstrates that the effective barrier for decaying from the HS to the LS state is not simply the barrier present in a single molecule. Rather, the collective interactions stabilize molecules in the same spin-state as others in their locality. This suggests that enhancing collective interactions is an important route to increasing T_{LIESST}. Our prediction is consistent with the behaviors observed in $[\mathrm{Fe_xMn_{1\text{-}x}(ptz)_6}](\mathrm{BF_6})_2$ and $\{[\mathrm{Zn_{1-}}_x\mathrm{Fe}_x(\mathrm{bbtr})_3](\mathrm{BF_4})_2\}_\infty$,[27,63] which show an increase in T_{LIESST} and hysteresis width with increased Fe concentration and hence increased interactions.

Furthermore, our simulations demonstrate that when collective interactions become im-

portant the HS→LS decay is non-exponential (figure S4) and shows significant deviations from the predictions for a single molecule in solution (equation S45). This is consistent with the experimental observation that the HS→LS becomes non-exponential when the interactions between SCO centers are important.[27,48,63]

Notice that the largest values of k_2 shown in figure 4 are small compared to those found in many materials, cf. table 1. This is because increasing k_2 (or k_1) also increases the hysteresis width of the thermal transition, figure S8. Again, this is consistent with $[Fe_xMn_{1-x}(ptz)_6](BF_6)_2$,[63] where the hysteresis increases with increased Fe concentration. Therefore, although strong cooperative interactions dramatically increase T_{LIESST} they also decrease $T_{1/2\uparrow}$. When the spin-state transition is highly cooperative (i.e., for large k_1 and/or k_2) trapped excited spin-states are stable to temperatures greater than the spin-state transition temperature on heating, $T_{\mathrm{LIESST}} > T_{1/2\uparrow}$. In this case a sample cooled from high temperatures remains in the HS state throughout the temperature sweep, figure 5a, but the LS state can is stable a low temperature following, for example, a reverse-LIESST experiment. This phenomenology has been seen in several experiments.[25–27] Thus, we predict that while strong cooperativity between SCO centers is a powerful strategy for enhancing T_{LIESST}, doing so will typically not result in straightforward SCO materials with high T_{LIESST}. Rather, in highly cooperative systems we predict that the HS state will remain stable to low temperatures but an extremely high $T_{\mathrm{r\text{–}LIESST}}$ will be found. Importantly, when $T_{\mathrm{LIESST}} > T_{1/2\downarrow}$ both the HS and LS states are stable below $T_{1/2\uparrow}$, that is $T_{\mathrm{r\text{–}LIESST}} = T_{1/2\uparrow}$. Hence, very large values of $T_{\mathrm{r\text{–}LIESST}}$ can be achieved. Therefore, highly cooperative systems that remain HS on thermal cycling, but allow for reverse-LIESST, are ideal platforms for achieving high temperature switching between long lived metastable states, as we demonstrate below.

For reasonable parameters $T_{\mathrm{r\text{–}LIESST}}$ can be pushed above room temperature in our model, figure 5a. This suggests that highly cooperative materials offer an extremely promising route to high-temperature switching. Reverse-LIESST can be used to switch to the LS phase, and LIESST to return to the HS phase. If both phases can be stabilized at room temperature,

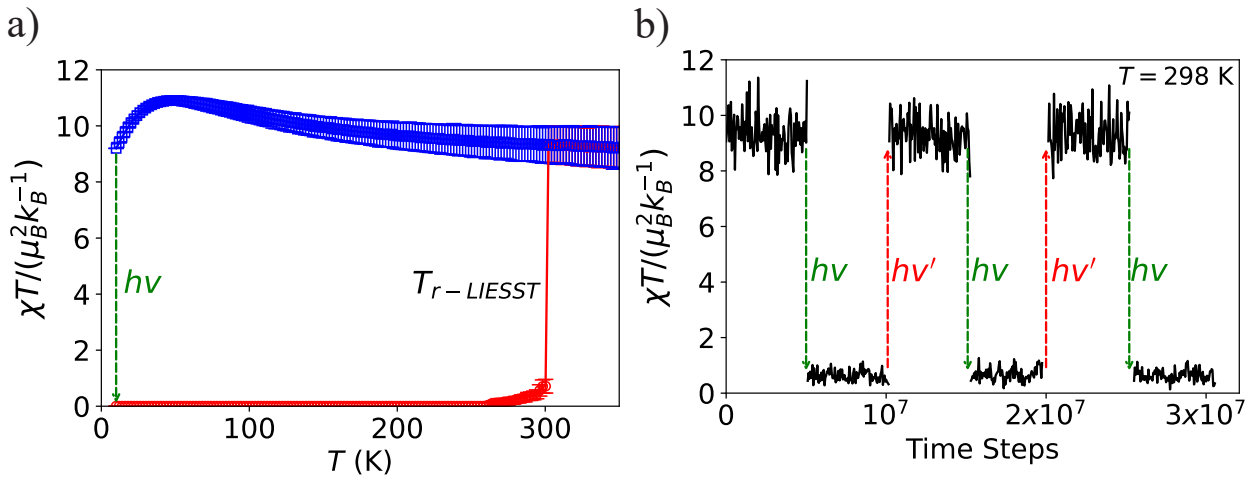

Figure 5: Room temperature switching in a strongly cooperative material. (a) An example of a system that remains in the HS phase on thermal cycling, but where the LS is stable for long times even above room temperature, i.e., $T_{\text{r–LIESST}} > 298$ K. Blue squares indicate data obtained by initializing at an all HS state at high temperature and cooling to 10 K whereas red circles indicate data obtained by initializing in an all LS state at 10 K and slowly heating. (b) Switching at 298 K. Black data shows the time evolution of the magnetic susceptibility at room temperature. The vertical red (green) arrows schematically indicate the light irradiation in a LIESST (resp. reverse-LEISST) experiment; in the calculation we reset the model to all HS (resp. LS) at these times. For these calculations $Dq/B = 2.054$, $\delta = 0.12$ Å, $k = 12$ eV/Å^2, $k_2 = 0.43$ eV/Å^2, and all other parameters take their default values.

then room temperature spin-state switching appears possible. To test this we simulated repeated LIESST/reverse-LIESST experiments at room temperature (298 K), figure 5b. We found that both states remain stable for long times and the timescale of our simulations exceeds what is practicable before we observe decay of either state.

Relatively little attention has been focused on how to enhance the cooperativity of SCO transitions. Nevertheless, the covalently bonded networks in framework materials would seem to offer a natural route to enhance cooperativity. Hence, exploring more rigid ligands in framework materials should be a priority. It is also worth noting that large ΔH will enhance $T_{\text{r–LIESST}}$ as this increases the barrier for a single molecule to decay from the LS state to the HS state.

Finally, we show that the spin-orbit coupling (ζ) has important and subtle influence on T_{LIESST}, figure 6. On one hand, increasing ζ introduces larger zero-field splitting between HS levels (figure S9), which results in higher T_{LIESST}. On the other hand, increasing ζ decreases the energy barrier, E_b, (figure S10), which lowers T_{LIESST}. These competing effects lead to maximum T_{LIESST} for intermediate values of ζ. $T_{1/2}$ is decreased by stronger spin-orbit coupling. This is primarily because the zero field splitting decreases the energy of several of the HS states, decreasing the enthalpy difference between the HS and LS states. It is notable that both of these effects are quite large, $\sim$ 50 K. This suggests that optimizing the spin orbit coupling could be a powerful route to increasing T_{LIESST}. The most obvious route to increase the spin-orbit coupling would be to move to heavier metals, but this may be difficult in practice as SCO is most common in 3d metals. However, the effective spin-orbit coupling is strongly modified by the ligand field, which is known as the relativistic nephelauxetic effect.[82] There are three major causes of the relativistic nephelauxetic effect: (a) the covalent mixing of the metal and ligand wavefunctions; (b) the expansion of the d-orbital of the metal (change in the radial wavefunction), related to forming a covalent bond with the ligand; and (c) the SOC of the ligand. Thus, we predict that ligands with high covalency and large ligand SOC constants (i.e., containing heavier atoms) will lead to

larger ζ and thus higher T_{LIESST}. Thus, Hoffman frameworks should provide fertile ground for materials with high T_{LIESST}.[25,97]

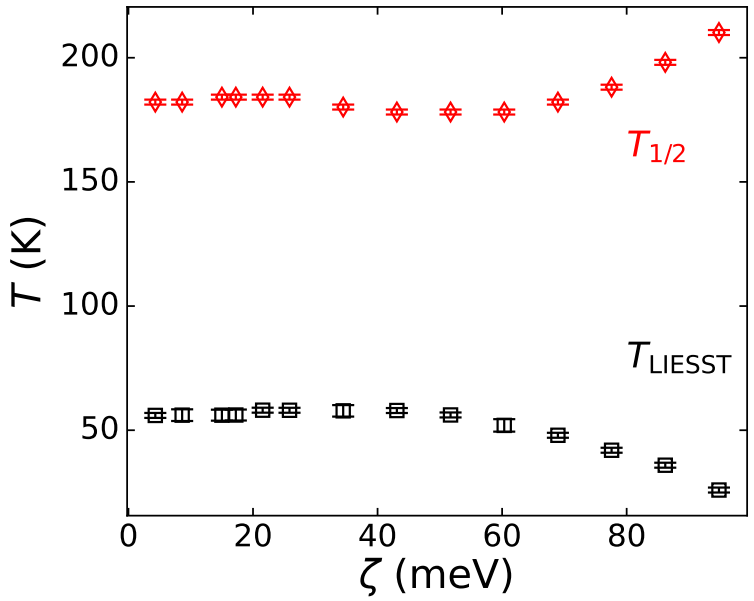

Figure 6: Effect of spin-orbit coupling strength ζ on T_{LIESST} and $T_{1/2}$. Other parameters have the default values given in table 1.

An important consequence of the relativistic nephelauxetic effect is that complexes with predominantly N and O ligation should have small effective spin-orbit coupling constants (ζ) as the ligand spin-orbit coupling effect is insignificant for light elements.[82] The results in figure 6 show that weak spin-orbit coupling strongly suppresses T_{LIESST}. As N and O are the most widely studied donor atoms in SCO complexes this may well be a significant factor limiting T_{LIESST}. Thus, we propose that utilizing heavier atoms in the inner coordination sphere may provide a new route to higher T_{LIESST}

Conclusion

We have introduced a microscopic model of SCO materials based on crystal-field theory including intra- and inter-molecular vibrations. We explicitly include the spin-orbit interaction that induces zero-field splittings within the HS manifold and the coupling between the HS

and LS states (via the IS state). This model provides a unified picture of thermal and light-induced spin-crossover. The calculated magnetic susceptibility is in striking agreement with experiments on SCO materials. Our theory reproduces and explains the inverse correlation between $T_{1/2}$ and T_{LIESST}, in excellent agreement with experimental data. It explains that the different T_0 values found in SCO materials with ligands with different denticities results from the increase in inner coordination sphere stiffness with denticity.

Two key goals, motivated by possible applications of SCO materials, are to increase T_{LIESST} and the width of the thermal hysteresis. T_{LIESST} can be increased by decreasing the ligand field strength to minimize the enthalpy difference between the HS and LS states (ΔH), increasing the stiffness of the inner coordination sphere or the stiffness of the bulk material, and optimizing the effective spin-orbit coupling via heavier atoms (particularly in the inner coordination sphere). Hysteresis width can be increased by increasing the cooperativity between molecules in the solid state. However, the most promising means to achieve room temperature switching is to enhance the cooperativity of the spin-state transition, such that the HS phase remains stable on thermal cycling, but that the LS phase can be populated by, for example, reverse-LIESST. In such materials both the HS and LS phases are (meta)stable at all temperatures below $T_{\mathrm{r\text{–}LIESST}}$ as $T_{\mathrm{LIESST}} > T_{1/2\downarrow}$ and $T_{\mathrm{r\text{–}LIESST}} = T_{1/2\uparrow}$.

We have shown that highly cooperative materials have particular promise for room temperature bistability. In particular, we found that our model allows room temperature switching in for reasonable parameters. Highly cooperative materials where the HS state remains stable on thermal cycling to low temperatures have clear advantages over switching in the thermal hysteresis loop because of the potential to massively increase the temperature range where bistability is found – a requirement for robust technologies that can operate in varied environmental conditions. Two complimentary strategies to enhance $T_{\mathrm{r\text{–}LIESST}}$ are to explore more rigid ligands in framework materials and systems with large ΔH. We emphasize the thermally-driven SCO is not required for high-temperature switching and that our results indicate that materials that do *not* display thermal SCO allow switching between long-lived

(meta)stable states to the highest temperatures.

Acknowledgments

It is a pleasure to acknowledge helpful conversations with Cameron Kepert, Ross McKenzie, Suzanne Neville, and Finnian Rist. This work was supported by the ARC through project DP200100305. M. Nadeem and G. Ruzzi were supported by an Australian Government Research Training Program Scholarship

Supporting Information Available

Mathematical description of the model

Low-energy model of a single SCO molecule

In the crystal-field theory of octahedral d^6 SCO molecules the crystal-field strength induces a splitting, $10Dq$, between the t_{2g} and e_g orbitals.[78] The overlap integrals of electronic interactions can be written in terms of the three Racah parameters: A, B, and C.[78] The terms proportional to A only depend on the total filling d orbitals, and so are constant if we limit ourselves to d^6-states, as we will below. The ratio B/C is found to be independent of both the atomic number and the number of electrons in the iron-group ions.[78] Therefore, we take the standard ratio[78] $B/C = 4.41$ for all of our calculations. With B/C and the number of d-electrons fixed the energies of the terms (in units of B) only depend on Dq/B; this insight enabled Tanabe-Sugano to draw their eponymous diagrams.[78]

The spin-orbit interaction mixes terms with a spin quantum number difference of ± 1. Eigenstates of the spin-orbit interaction can be characterized by the irreducible representations of the octahedral double group $\overline{O}_h$, which has twice the number of symmetry elements as the usual octahedral group, O_h.[79] There is only non-zero spin-orbit coupling between states that belong to the same representation of the double group. We consider only the three lowest energy terms $^1A_1$, $^3T_1$, and $^5T_2$, which we henceforth dub low-spin (LS), intermediate-spin (IS), and high-spin (HS) respectively. We show here that these three states contain the essential physics describing the dynamics of spin-crossover materials once they are prepared in some macroscopic state. The only representation of the double group that appears in both the HS and LS manifolds is the trivial representation ($\overline{A}_1$), thus only spin-orbit coupling between these states can allow spin-crossover in strictly octahedral molecules. However as the total spin of the LS and HS states differs by 2, this must be mediated via the $\overline{A}_1$ IS state,[44] as sketched in figure S1. Even considering nearly octahedral molecules or includ-

ing vibrational distortions away from perfect octahedrality will only lead to weaker effects (formally higher order in a small parameter measuring the deviation from perfect octahedrality). Therefore, this result is, to a good approximation, true quite generally. For simplicity, we neglect the spin-orbit coupling only between the non-trivial representations of IS and HS levels, as this will only have a small quantitative effect on the results below. However, spin-orbit coupling splits the IS and HS terms into levels with total angular momentum of $j = 0, 1, 2$ and $j = 1, 2, 3$ respectively, we retain this zero-field splitting as it has important (qualitative) consequences for experiments on SCO materials, particularly measurements of their magnetic susceptibility.

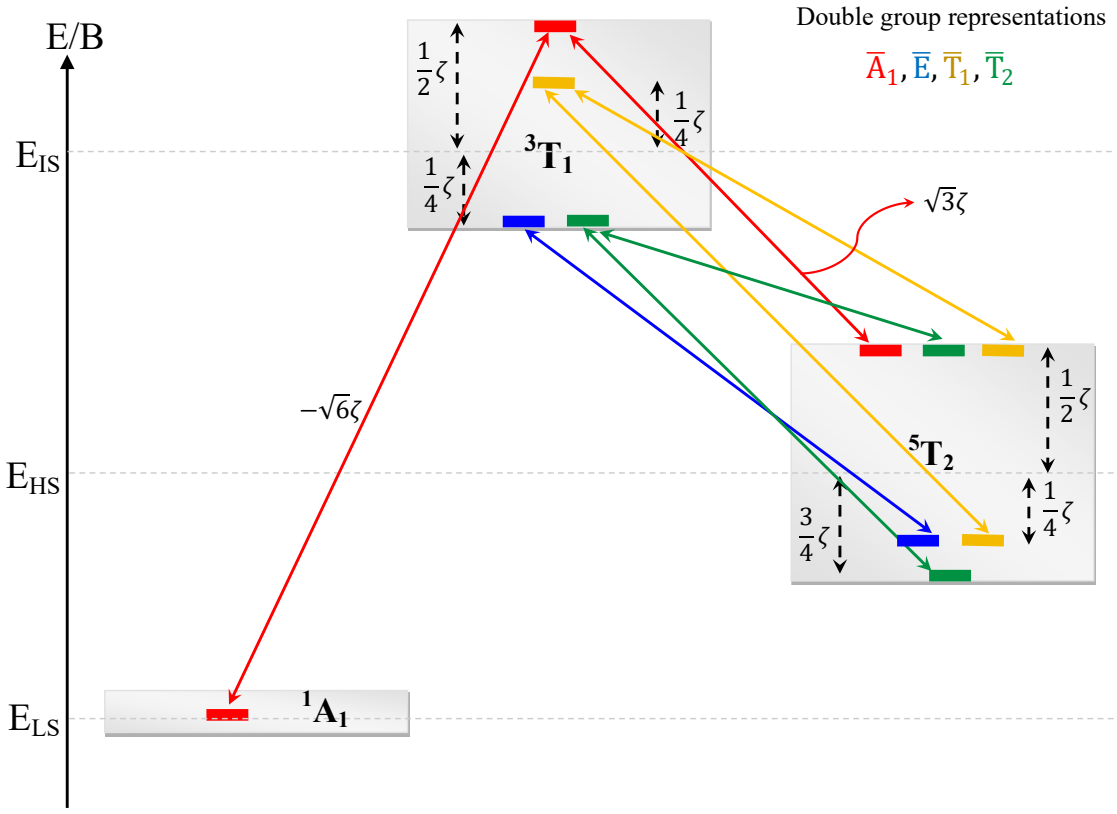

Figure S1: Schematic energy diagram of the three lowest energy electronic terms of d^6 and the effect of spin-orbit interaction in the region of the Tanabe-Sugano diagram relevant to SCO (where the $^1A_1$ term has slightly lower energy than the $^5T_2$ term). The superscript is the spin multiplicity $(2S + 1)$ of the term, where S is the total spin quantum number. A_1, T_1 and T_2 are the irreducible representation of O_h having orbital degenracies of 1, 3 and 3 respectively. The arrows indicate the spin-orbit couplings between the states.[79]

We explicitly add the symmetric vibration of the metal-ligand bonds to the usual crystal-field treatment. Thus, the Hamiltonian in the basis of the double group representations is

$$\begin{aligned} H_1 =& \sum_{\alpha} \sum_{j \in \alpha} \sum_{\overline{\Gamma} \in \alpha} \sum_{\gamma=0}^{N_{\overline{\Gamma}}-1} \left(V_{\alpha j}(Q) + \frac{P^2}{2M} \right) \left| \alpha, j, \overline{\Gamma}, \gamma \right\rangle\!\!\left\langle \alpha, j, \overline{\Gamma}, \gamma \right| \\ &+ \zeta \Big\{ \sqrt{3} \left| \mathrm{LS}, 0, \overline{A}_1, 0 \right\rangle \left\langle IS, 0, \overline{A}_1, 0 \right| - \sqrt{6} \left| \mathrm{HS}, 3, \overline{A}_1, 0 \right\rangle \left\langle IS, 0, \overline{A}_1, 0 \right| + h.c. \Big\}, \end{aligned} \tag{S1}$$

where Q is the difference of the metal-ligand bond length from the minimum energy bond length in the IS state, P and M are the associated momentum and mass respectively, $V_{\alpha j}$ is the potential energy surface for states of term α with total angular momentum j, ζ is the spin-orbit coupling constant, $\left| \alpha, j, \overline{\Gamma}, \gamma \right\rangle$ is a state within term α with total angular momentum j and double group representation $\overline{\Gamma}$, with γ enumerating the $N_{\overline{\Gamma}}$-fold degeneracy of $\overline{\Gamma}$, and $h.c.$ is hermitian conjugate.

We assume that Q can be treated classically. Thus, the theory developed here will miss the low temperature saturation of the HS decay rate due to quantum nuclear tunneling[29,44,45] [i.e., $k(T \to 0) \to \infty$ in our theory]. However, we expect the effects of this approximation to be small for the results described below as we focus on the high temperature thermally activated regime, $T \gtrsim T_{\mathrm{LIESST}}$.

We assume harmonic potential energy surfaces,

$$V_{\alpha j}(Q) = E_{\alpha} + \zeta_{\alpha,j} + k_{\alpha} \big(Q - Q_{\alpha}^{(0)} \big)^2, \tag{S2}$$

where E_{α} is the energy of term α (i.e., the energy plotted in Tanabe-Sugano diagrams), which depends on Dq and B, $\zeta_{\alpha,j}$ is the zero-field splitting induced by the spin-orbit coupling for states with total angular momentum j in term α, and k_{α} and $Q_{\alpha}^{(0)}$ are respectively the spring constant and minimum energy bond length for the symmetric metal-ligand mode when the molecule is in an electronic state in term α. k_{α} and $Q_{\alpha}^{(0)}$ are assumed to be independent of j. To account for difference in the bond length between the HS and LS states (2δ), we set

$Q_{\mathrm{HS}}^{(0)} = \delta$, $Q_{\mathrm{IS}}^{(0)} = 0$ and $Q_{\mathrm{LS}}^{(0)} = -\delta$; and to account the softening of the metal-ligand bond that accompanies a spin transition, we set $k_{\mathrm{LS}} = k + \kappa$, $k_{\mathrm{IS}} = k$ and $k_{\mathrm{HS}} = k - \kappa$. Typical potential energy surfaces for this model are shown in figure 1a.

We will not explicitly include the asymmetric modes, but neither can they be entirely neglected as they have two crucial effects for SCO molecules. Firstly, their softening in the HS state is the leading contribution to the entropy difference (ΔS) between LS and HS states.[86] The temperature dependence of ΔS is determined by the frequency shifts on SCO of all asymmetric molecular modes.[98] For simplicity we model the entropy difference instead with all fourteen asymmetric metal-ligand modes having the same "average frequency", that takes the values ω_{LS} and ω_{HS} in the HS and LS states respectively, and assume the SCO does not shift the other (ligand only) molecular modes, as these are believed to contribute very weakly to ΔS.[99] Note that the entropy changes due to the softening of the symmetric mode and the changes in spin and orbital degeneracy are explicitly included in our model and therefore are not included in the ΔS term. Thus,

$$\Delta S(T) = 14\left(\frac{\hbar\omega_{\mathrm{HS}}}{T}\frac{1}{\exp\left(\frac{\hbar\omega_{\mathrm{HS}}}{k_B T}\right)-1} - \frac{\hbar\omega_{\mathrm{LS}}}{T}\frac{1}{\exp\left(\frac{\hbar\omega_{\mathrm{LS}}}{k_B T}\right)-1} + k_B \ln\left[\frac{1-\exp\left(-\frac{\hbar\omega_{\mathrm{LS}}}{k_B T}\right)}{1-\exp\left(-\frac{\hbar\omega_{\mathrm{HS}}}{k_B T}\right)}\right]\right). \tag{S3}$$

Following Wajnflasz and Pick[69] we absorb the entropy of the asymmetric modes to the Hamiltonian.

Secondly, asymmetric vibrational distortions allow for thermally induced transitions between the different double group representations within, e.g., the HS term as they lower the symmetry of the molecule. We include this in our model by assuming that these transitions are barrierless and therefore the internal population of states within the HS manifold tends to rapidly reach thermal equilibrium. We achieve this in the numerical calculations via a Monte Carlo procedure, described in the methods section.

Canonical transformation

General theory for non-degenerate low-energy spaces

While the theory is standard for degenerate low-energy states, we are not aware of a detailed presentation of the non-degenerate case,[91–93] so we start by giving one. Consider an arbitrary Hamiltonian, $H = H_0 + H_1$ where $H_0 = \sum_\nu P_\nu H P_\nu$, $H_1 = \sum_{\mu\neq\nu} P_\nu H P_\mu$, and P_ν is a projector onto the νth subspace. Now define $H(\varepsilon) = H_0 + \varepsilon H_1$. Let

$$\begin{aligned} \overline{H}(\varepsilon) &\equiv e^{-i\varepsilon S} H(\varepsilon) e^{i\varepsilon S} && \text{(S4)} \\ &= H_0 + \varepsilon\left(H_1 + i\left[H_0, S\right]\right) + \frac{\varepsilon^2}{2}\left(2i\left[H_1, S\right] - \left[\left[H_0, S\right], S\right]\right) + \ldots && \text{(S5)} \end{aligned}$$

We choose S so that the linear term vanishes, i.e., such that

$$iH_1 = \left[H_0, S\right]. \tag{S6}$$

Therefore,

$$\overline{H} \equiv \overline{H}(1) = H_0 + \frac{i}{2}\left[H_1, S\right]. \tag{S7}$$

Note that $P_\mu P_\nu = P_\mu \delta_{\mu\nu}$ and $\sum_\mu P_\mu = 1$. Thus, it follows from Eq. (S6) that

$$\begin{aligned} 0 &= P_\mu H_1 P_\nu + i P_\mu H_0 S P_\nu - i P_\mu S H_0 P_\nu && \text{(S8)} \\ &= \sum_{\mu'\neq\nu'} P_\mu P_{\mu'} H P_{\nu'} P_\nu + i \sum_{\mu'} P_\mu P_{\mu'} H P_{\mu'} S P_\nu - i \sum_{\mu'} P_\mu S P_{\mu'} H P_{\mu'} P_\nu && \text{(S9)} \\ &= P_\mu H P_\nu (1 - \delta_{\mu\nu}) + i P_\mu H P_\mu (P_\mu S P_\nu) - i (P_\mu S P_\nu) P_\nu H P_\nu. && \text{(S10)} \end{aligned}$$

For $\mu \neq \nu$ we find

$$iP_\mu H P_\nu = P_\mu H P_\mu (P_\mu S P_\nu) - (P_\mu S P_\nu) P_\nu H P_\nu \tag{S11}$$

$$\simeq \langle P_\mu H P_\mu \rangle (P_\mu S P_\nu) - (P_\mu S P_\nu) \langle P_\nu H P_\nu \rangle, \tag{S12}$$

which implies that

$$P_\mu S P_\nu \simeq \frac{i P_\mu H P_\nu}{\langle P_\mu H P_\mu \rangle - \langle P_\nu H P_\nu \rangle}. \tag{S13}$$

While, for $\mu = \nu$ we find

$$P_\mu H P_\mu (P_\mu S P_\mu) = (P_\mu S P_\mu) P_\mu H P_\mu, \tag{S14}$$

which implies that

$$P_\mu S P_\mu = \gamma P_\mu \tag{S15}$$

for $\gamma \in \mathbb{C}$.

Thus we have

$$\overline{H} = \sum_{\mu} P_\mu H P_\mu + \frac{i}{2}\sum_{\mu\neq\nu}\sum_{\mu'\nu'}(P_\mu H P_\nu P_{\nu'} S P_{\mu'} - P_{\mu'} S P_{\nu'} P_\mu H P_\nu) \tag{S16}$$

$$= \sum_{\mu} P_\mu H P_\mu + \frac{i}{2}\sum_{\mu\neq\nu}\sum_{\mu'}(P_\mu H P_\nu P_{\mu'} S P_{\mu'} - P_{\mu'} S P_{\mu'} P_\mu H P_\nu) + \frac{i}{2}\sum_{\mu\neq\nu}\sum_{\mu'\neq\nu'}(P_\mu H P_\nu P_{\nu'} S P_{\mu'} - P_{\mu'} S P_{\nu'} P_\mu H P_\nu) \tag{S17}$$

$$\simeq \sum_{\mu} P_\mu H P_\mu + \frac{i}{2}\sum_{\mu\neq\nu}(\gamma P_\mu H P_\nu - \gamma P_\mu H P_\nu) - \frac{1}{2}\sum_{\mu\neq\nu}\sum_{\mu'\neq\nu'}\left(\frac{P_\mu H P_\nu P_{\nu'} H P_{\mu'}}{\langle P_{\nu'} H P_{\nu'}\rangle - \langle P_{\mu'} H P_{\mu'}\rangle} - \frac{P_{\mu'} H P_{\nu'} P_\mu H P_\nu}{\langle P_{\mu'} H P_{\mu'}\rangle - \langle P_{\nu'} H P_{\nu'}\rangle}\right) \tag{S18}$$

$$= \sum_{\mu} P_\mu H P_\mu - \frac{1}{2}\sum_{\mu\neq\nu}\sum_{\mu'\neq\nu}\left(\frac{P_\mu H P_\nu H P_{\mu'}}{\langle P_\nu H P_\nu\rangle - \langle P_{\mu'} H P_{\mu'}\rangle} + \frac{P_\mu H P_\nu H P_{\mu'}}{\langle P_\nu H P_\nu\rangle - \langle P_\mu H P_\mu\rangle}\right) \tag{S19}$$

$$= \sum_{\mu} P_\mu H P_\mu - \frac{1}{2}\sum_{\mu\neq\nu}\sum_{\mu'\neq\nu} P_\mu H P_\nu H P_{\mu'}\left(\frac{1}{\langle P_\nu H P_\nu\rangle - \langle P_{\mu'} H P_{\mu'}\rangle} + \frac{1}{\langle P_\nu H P_\nu\rangle - \langle P_\mu H P_\mu\rangle}\right) \tag{S20}$$

First let us consider the case where we are only interested in the effective Hamiltonian in the low-energy subspace defined by $\mu = 0$ – we have

$$H_{\text{eff}} = P_0 \overline{H} P_0 \tag{S21}$$

$$= P_0 H P_0 - \frac{1}{2}\sum_{\nu\neq 0}\left(\frac{P_0 H P_\nu H P_0}{\langle P_\nu H P_\nu\rangle - \langle P_0 H P_0\rangle} - \frac{P_0 H P_\nu H P_0}{\langle P_0 H P_0\rangle - \langle P_\nu H P_\nu\rangle}\right) \tag{S22}$$

$$= P_0\left(H - \sum_{\nu\neq 0}\frac{P_0 H P_\nu H P_0}{\langle P_\nu H P_\nu\rangle - \langle P_0 H P_0\rangle}\right), \tag{S23}$$

consistent with straightforward perturbation theory.

Alternatively consider the case where we care about states with different energies within the low-energy subspace, henceforth denoted $\mathcal{L}$. Here it is convenient work in a basis chosen so that the low energy subspace is diagonal, i.e., $P_\mu H P_\nu = 0$ if both μ and $\nu \in \mathcal{L}$. (This is always possible provided we can solve the problem restricted purely to $\mathcal{L}$, which is reminiscent

of degenerate perturbation theory.) We then find that

$$\begin{aligned} H_{\text{eff}} &\equiv P_{\mathcal{L}}\overline{H}P_{\mathcal{L}} \\ &= \sum_{\mu\in\mathcal{L}} P_\mu H P_\mu - \frac{1}{2}\sum_{\mu,\mu'\in\mathcal{L}}\sum_{\nu\notin\mathcal{L}}\left(\frac{P_\mu H P_\nu H P_{\mu'}}{\langle P_\nu H P_\nu\rangle - \langle P_{\mu'} H P_{\mu'}\rangle} + \frac{P_\mu H P_\nu H P_{\mu'}}{\langle P_\nu H P_\nu\rangle - \langle P_\mu H P_\mu\rangle}\right), \end{aligned} \tag{S24}$$

where $P_{\mathcal{L}} = \sum_{\mu\in\mathcal{L}} P_\mu$.

Application to model of SCO complexes

In the present work we choose $\mathcal{L}$ to contain the LS and all HS states and then integrate out the IS states. In principle other intermediate spin terms could be included in this transformation, however this would only lead to small quantitative changes in our results, which are not of interest here as we do not know the model parameters accurately for individual materials in any case. The canonical transformation results in an effective Hamiltonian given by

$$\begin{aligned} \tilde{H}_1 = &\sum_{\mu=\widetilde{\text{LS}},\widetilde{\text{HS}}}\left(V_\mu(Q) + \frac{P^2}{2M}\right)|\mu\rangle\langle\mu| + \lambda\left\{\left|\widetilde{\text{LS}}\right\rangle\left\langle\widetilde{\text{HS}}\right| + H.C.\right\} - T\Delta S\left|\widetilde{\text{HS}}\right\rangle\left\langle\widetilde{\text{HS}}\right| \\ &+ \sum_{\overline{\Gamma}\neq\overline{A}_1}\sum_{j,\gamma}\left(V_{\text{HS},j}(Q) + \frac{P^2}{2M} - T\Delta S\right)|HS,j,\overline{\Gamma},\gamma\rangle\langle HS,j,\overline{\Gamma},\gamma|, \end{aligned} \tag{S25}$$

where the 'dressed' low-energy electronic states are

$$\left|\widetilde{\text{LS}}\right\rangle = |\text{LS},0,A_1,0\rangle + \frac{\sqrt{6}\zeta}{V_{\text{IS},0}(Q) - V_{\text{LS},0}(Q)}|\text{IS},0,A_1,0\rangle, \tag{S26}$$

$$\left|\widetilde{\text{HS}}\right\rangle = |\text{HS},3,A_1,0\rangle - \frac{\sqrt{3}\zeta}{V_{\text{IS},0}(Q) - V_{\text{HS},3}(Q)}|\text{IS},0,A_1,0\rangle, \tag{S27}$$

the effective coupling between the low-energy states is

$$\lambda(Q) = \frac{3\zeta^2}{\sqrt{2}}\left(\frac{1}{V_{\text{IS},0}(Q) - V_{\text{LS},0}(Q)} + \frac{1}{V_{\text{IS},0}(Q) - V_{\text{HS},3}(Q)}\right), \tag{S28}$$

and the potential energies surfaces for these two low energy states are

$$V_{\widetilde{\mathrm{HS}}}(Q) = V_{\mathrm{HS},3}(Q) - \frac{3\zeta^2}{V_{\mathrm{IS},0}(Q) - V_{\mathrm{HS},3}(Q)} \tag{S29}$$

and

$$V_{\widetilde{\mathrm{LS}}}(Q) = V_{\mathrm{LS},0}(Q) - \frac{6\zeta^2}{V_{\mathrm{IS},0}(Q) - V_{\mathrm{LS},0}(Q)}. \tag{S30}$$

We diagonalize the potential terms in Hamiltonian S25 in the adiabatic limit. $\widetilde{\mathrm{HS}}$ and $\widetilde{\mathrm{LS}}$ are mixed and give a double well (DW) ground state potential with two local minima, corresponding to HS and LS states, and a high energy state, which we neglect. The DW state is

$$|\mathrm{DW}\rangle = \sin[\theta(Q)] \left|\widetilde{\mathrm{LS}}\right\rangle + \cos[\theta(Q)] \left|\widetilde{\mathrm{HS}}\right\rangle, \tag{S31}$$

where

$$\tan[2\theta(Q)] = \frac{2\lambda(Q)}{V_{\widetilde{\mathrm{HS}}}(Q) - V_{\widetilde{\mathrm{LS}}}(Q)}. \tag{S32}$$

The potential energy surface of the DW state is given by

$$V_{DW}(Q) = \frac{V_{\widetilde{\mathrm{HS}}}(Q) + V_{\widetilde{\mathrm{LS}}}(Q)}{2} - \sqrt{\left(\frac{V_{\widetilde{\mathrm{HS}}}(Q) - V_{\widetilde{\mathrm{LS}}}(Q)}{2}\right)^2 + \lambda^2}. \tag{S33}$$

This potential is plotted, for typical parameters, in figure 1b. The DW state is somewhat similar to the potential, introduced on phenonomenogical grounds, by Nishino *et al.*, in order to study the nonmonotonic thermal expansion of SCO materials.[100]

The spin quantum number S in the DW state is obtained from $\langle S^2(Q)\rangle = S(S+1)$, where

$$\begin{aligned}
\langle S^2(Q)\rangle &= 6\,|\langle \mathrm{HS},3,A_1,0|\mathrm{DW}\rangle|^2 + 2\,|\langle IS,0,A_1,0|\mathrm{DW}\rangle|^2 \\
&= 6\cos^2[\theta(Q)]\frac{[V_{\mathrm{IS},0}(Q) - V_{\mathrm{HS},3}(Q)]^2 + \zeta^2}{[V_{\mathrm{IS},0}(Q) - V_{\mathrm{HS},3}(Q)]^2} + \sin^2[\theta(Q)]\frac{12\zeta^2}{[V_{\mathrm{IS},0}(Q) - V_{\mathrm{LS},0}(Q)]^2} \\
&\quad + \sin[2\theta(Q)]\frac{3\sqrt{2}\zeta^2}{[V_{\mathrm{IS},0}(Q) - V_{\mathrm{HS},3}(Q)][V_{\mathrm{IS},0}(Q) - V_{\mathrm{LS},0}(Q)]}.
\end{aligned} \tag{S34}$$

S is strongly Q dependent, as shown in figure S2.

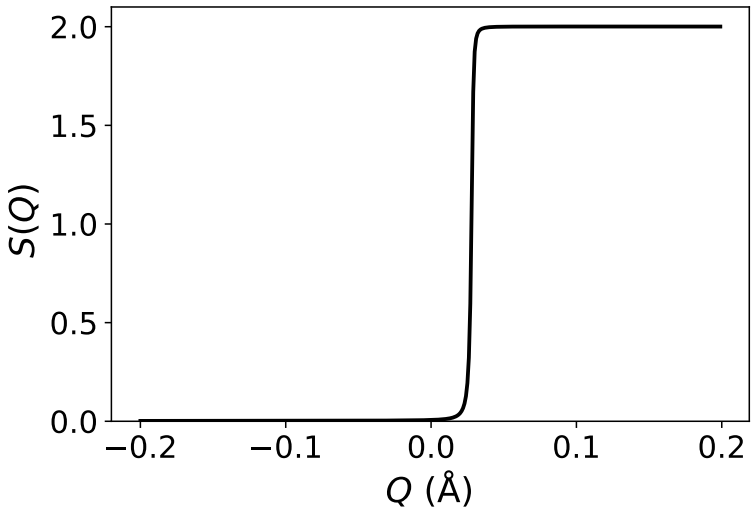

Figure S2: Spin of the DW state as function of metal ligand bond length Q at $T = 0$ K. All parameters have their default values, given in table 1.

Thus, we arrive at a simple classical model for a single SCO molecule given by

$$H_1^{\text{eff}} = V_\nu(Q) + \frac{P^2}{2M}, \tag{S35}$$

where the index ν runs from 0 to 14, with $V_0(Q) = V_{DW}(Q)$ and V_1 through V_{14} equaling the fourteen pure HS states (the ordering is unimportant), as shown in figure 1b, with hopping allowed between the potential energy surfaces.

Inter-molecular elastic interactions

To describe the collective behaviors of molecular SCO crystals and SCO frameworks, we include an elastic interaction between nth nearest neighboring molecules, $U_n(Q_i, Q_j, \mathbf{r}_i, \mathbf{r}_j)$. As we assume that this is mediated via the ligands the interaction depends on both the positions of the molecules, $\mathbf{r}_i$ and $\mathbf{r}_j$, and their internal coordinates, Q_i and Q_j. Here we consider a square lattice with the interaction between nearest and next nearest neighbors

given by

$$U_n(Q_i, Q_j, \mathbf{r}_i, \mathbf{r}_j) = \frac{k_n}{2}\big(|\mathbf{r}_i - \mathbf{r}_j| - \sqrt{n}\{2\bar{d} + Q_i + Q_j\}\big)^2. \tag{S36}$$

where k_n is the force constant between nth nearest neighbors and $2\bar{d}$ is the equilibrium distance between the 1st nearest neighbors at $Q_i = Q_j = 0$. The effective model must also include the kinetic energy of the center of mass of the molecule and a copy of the single molecule effective Hamiltonian for every molecule. This yields

$$H = \sum_i^N \left[\frac{\mathbf{p}_i^2}{2m} + \frac{P_i^2}{2M} + V_{\nu_i}(Q_i) + \sum_{\langle i,j\rangle_{1,2}} U_n(Q_i, Q_j, \mathbf{r}_i, \mathbf{r}_j) \right], \tag{S37}$$

where, $\mathbf{p}_i$ and m are the momentum and mass respectively of the molecule, and a subscript, i, has been added to the single molecule variables P_i, ν_i, and Q_i to differentiate the terms on different molecules.

Magnetic Susceptibility

As we assume there are no magnetic interactions between the SCO centers, the magnetization at a temperature T is the sum over N sites. Our single molecule model, equation S35, has fifteen internal states as shown in figure 1b, with all states being pure HS except for the DW state. Computationally, we take a molecule on the DW potential to be HS if $|\langle \mathrm{HS}, 3, A_1, 0|\mathrm{DW}\rangle|^2 \geq \rho$, where ρ is a random number on the interval $[0, 1]$. The magnetization of a molecule in the LS state is zero and in the HS state it is[98]

$$M_i = \sum_{\{j,\bar{\Gamma},\gamma\}\in HS} \left\langle n_{i,j,\bar{\Gamma},\gamma}(Q_i(t), t) \left[-\frac{\partial V_{j,\bar{\Gamma},\gamma}(Q_i(t))}{\partial B} \right] \right\rangle_t, \tag{S38}$$

where $\langle \dots \rangle_t$ is the ensemble average over the simulation time and $n_{i,j,\bar{\Gamma},\gamma}(Q_i(t), t)$ is the occupation of state $\left|\mathrm{HS}, j, \bar{\Gamma}, \gamma\right\rangle$ of molecule i at time t (recall that in the DW state the probability that the state is a a HS state depends on Q_i). We exploit the degeneracy of the problem to write $n_{i,j,\bar{\Gamma},\gamma}(Q_i(t), t) = n_{i,j}(Q_i(t), t)/g_j$, where g_j is the degeneracy of the

HS state with total angular momentum j. This allows us to reduce the number of pure HS states explicitly simulated from 14 to 3, see Fig. 1. Note that in the DW state this becomes $n_{i,DW,A_{1g},1}(Q_i) = n_{i,DW}(Q_i)\cos[\theta(Q_i)]$ as $g_{\mathrm{DW}} = 1$ but we need to account for the probability of the DW being HS, see equation S31.

For paramagnetic ions with a Zeeman coupling to a weak magnetic field along z-axis B_z, the magnetic susceptibility is given, to second order in B_z, by[79]

$$\begin{aligned}\chi(T;\{Q_i\}) &= \lim_{B\to 0}\sum_{i=1}^{N}\frac{\partial M_i(Q_i)}{\partial B} \\ &= \left\langle \sum_{i=1}^{N}\sum_{\{j,\bar{\Gamma},\gamma\}\in HS}\left(\frac{\mu_B^2|\left\langle \mathrm{HS},j,\bar{\Gamma},\gamma\right| L_z+2S_z\left|\mathrm{HS},j,\bar{\Gamma},\gamma\right\rangle|^2}{\hbar^2 k_B T}\right.\right. \\ &\quad \left.\left. +2\left(\frac{\mu_B}{\hbar}\right)^2\sum_{j',\bar{\Gamma}',\gamma'}\frac{|\left\langle \mathrm{HS},j',\bar{\Gamma}',\gamma'\right| L_z+2S_z\left|\mathrm{HS},j,\bar{\Gamma},\gamma\right\rangle|^2}{V_{\mathrm{HS},j'}(Q_i)-V_{\mathrm{HS},j}(Q_i)}\right)\frac{n_{i,j}(Q_i(t),t)}{g_i}\right\rangle_t .\end{aligned} \tag{S39}$$

Molecular dynamics equations of motion

In the canonical or NVT ensemble the equations of motion (in scaled position coordinates $\mathbf{r}'_i = \frac{1}{V^{1/d}}\mathbf{r}_i$) and real-time[96] are

$$\ddot{\mathbf{r}}'_i = -\frac{1}{mV^{1/d}}\sum_{n=1}^{2}\frac{\partial U_n(Q_i,Q_{i+n},\mathbf{r}_i,\mathbf{r}_{i+n})}{\partial \mathbf{r}_i}+\left(\frac{\dot{s}_r}{s_r}+\frac{\dot{V}}{V}\right)\dot{\mathbf{r}}'_i, \tag{S40}$$

$$\ddot{\mathbf{Q}}_i = \frac{1}{M}\left(\frac{\partial V_{\nu_i}}{\partial Q_i}+\sum_{n=1}^{2}\frac{\partial U_n(Q_i,Q_{i+n},\mathbf{r}_i,\mathbf{r}_{i+n})}{\partial Q_i}\right)+\frac{\dot{s}_Q}{s_Q}\dot{Q}, \tag{S41}$$

$$\ddot{s}_r = \frac{\dot{s}_r^2}{s_r}\left(mV^{2/d}\sum_i^N \dot{\mathbf{r}}_i'^2 - dNT\right)\frac{s_r}{M_{s_r}}, \tag{S42}$$

$$\ddot{s}_Q = \frac{\dot{s}_Q^2}{s_Q}\left(M\sum_i^N \dot{Q}_i^2 - NT\right)\frac{s_Q}{M_{s_Q}}, \tag{S43}$$

$$\ddot{V} = \frac{\dot{s}_r \dot{V}}{s_r} + \frac{s_r^2}{dM_V V}\left(mV^{2/d} \sum_i^N \dot{\mathbf{r}}_i'^2 + V^{1/d} \sum_i^N \sum_{n=1}^2 \frac{\partial U_n(Q_i, Q_{i+n}, \mathbf{r}_i, \mathbf{r}_{i+n})}{\partial \mathbf{r}_i} . \mathbf{r}_i' - dP_{\text{ext}} V \right), \tag{S44}$$

where V is the unit cell volume, m_v is the mass associated with the volume variable V, s_r and s_Q are the thermostat variables for the position and internal coordinates respectively, and m_{s_r} and m_{s_Q} are their masses, d is the number of dimensions of the lattice, which we set to two here, T is temperature, P_{ext} is external pressure, which we set to zero in the calculations presented here, and the sums over n are to be read as including all nth nearest neighbors.

Definition of and error analysis for $T_{\mathbf{LIESST}}$ and $T_{1/2}$

Following the standard experimental protocol[65] we calculate $\partial \chi T / \partial T$ and define T_{LIESST} as the minimum of the derivative. The uncertainty in the minimum is calculated through error propagation of the standard deviations of the χT data points. The total error in the measurement of T_{LIESST} convolutes the uncertainties in the minimum and the temperature step of a simulation. We set the uncertainty due to the temperature step equal to half of the step size.

For a measurement of $T_{1/2}$, we interpolate a simulated $\langle S(T) \rangle$ data and find the temperature at which $\langle S(T_{1/2}) \rangle = 1$. For a case with thermal hysteresis, $T_{1/2\uparrow}$ is defined as the temperature at which half of the sample is switched from the LS to HS state on heating, whereas $T_{1/2\downarrow}$ is defined as the temperature at which half of the sample is switched from the HS to LS state on cooling. Moreover $T_{1/2} = (T_{1/2\uparrow} + T_{1/2\downarrow})/2$. The total error in the measurement of $T_{1/2}$ takes into account the uncertainties in finding $\langle S(T_{1/2}) \rangle = 1$ and the temperature step of the simulation. The uncertainty in $\langle S(T_{1/2}) \rangle = 1$ is calculated through error propagation of the standard deviations of the $\langle S(T) \rangle$ data points.

Simulation Scheme

1. We initialize the system with a specified pattern of HS or LS molecules at a fixed temperature. Here we studied either all HS or all LS initial states. We initialize a site at $Q_i = -\delta$ if it is in LS state and $Q_i = \delta$ if its is in a HS state. For an all HS state we run 1000 Monte-Carlo steps to define the thermal occupation of each HS level at the initial conditions. Initial velocities are chosen randomly from the Boltzmann distribution at the given temperature.

2. We use NPT molecular dynamics to let the system evolve for 50 time steps and determine the new configuration of the system.

3. We employ 20 Monte Carlo steps per site to equilibrate the internal potentials.

4. We repeat steps 2 and 3 for 10 000 iterations to achieve equilibration.

5. For the measurements of the average quantities such as χT and their standard deviation, we run the steps 2 and 3 for 2000 iterations.

6. The next temperature step is initialized with the final configuration of the previous step and we perform steps 2 through 5 again.

7. Once we have simulate the thermal evolution of χT and $\langle S \rangle$. We calculate T_{LIESST} and $T_{1/2}$ and their uncertainties.

Model Parameters

For free Fe(II) ion Racah parameter $B = 131.12$ meV.[44] In a ligand field, the nephelauxetic effect reduces B to $70 - 80\%$ of the free ion value.[80] We vary Dq such that the energy difference between the HS and LS states is in the range of $50 - 200$ meV – typical for SCO molecules.[101,102]

For a free Fe(II) ion, the experimentally estimated value of ζ is 49.6 meV.[81] However, the relativistic nephelauxetic effect can reduce ζ to less than half of the free ion value.[82] A DFT study of an Fe(II) spin-crossover compound has estimated that the spin-orbit coupling between the LS and IS states,[83] suggesting that ζ can go as low as 1.94 meV.

Typical spring constants for metal-ligand bond vary in the range of $5 - 15$ eVÅ^{-2}.[84,85] The frequencies of the symmetric Fe-ligand vibrational modes are typically a factor of 1.15-2.0[87,103] larger in the LS state than they are in the HS state. Assuming the effective mass involved does not change, this corresponds to k_{LS} being a factor of k_{LS} 1.3–4.0 larger than k_{HS}. Typical values of κ follow from the estimates of k and $k_{\mathrm{LS}}/k_{\mathrm{HS}}$.

For d^6 SCO compounds, the difference in HS and LS bond length (2δ) is found experimentally to be in the range of $0.16 - 0.30$ Å.[87,88]

We set the ω_{LS} and ω_{HS} to typical frequencies for the symmetric breathing mode for which the several measurements are available in the literature, summarized in table S1.

Estimates of typical near neighbor inter-molecular spring constant,s k_1 and k_2, for solid state SCO complexes have previously been made on the basis of the measured bulk and shear moduli and thermodynamics.[89,90]

Molecules in solution or dilute solids

If one only considers the DW potential and no interactions between molecules a simple Marcus-Hush type calculation[104] for the DW potential shows that for small ζ and κ the HS→LS decay rate is given by

$$k_{HS\to LS} = \frac{2\pi}{\hbar}\frac{|\lambda(0)|^2}{\sqrt{2k\delta^2 k_B T}}\exp\left(-\frac{(2k\delta^2-\Delta H)^2}{8k\delta^2 k_B T}\right), \tag{S45}$$

where $\lambda(0)$ is the effective spin orbit coupling in the IS geometry, defined in equation S28. Note that this yields $E_b = (2k\delta^2-\Delta H)^2/8k\delta^2$, suggesting that the energy barrier between the HS and LS states, and hence T_{LIESST}, is maximized for $\Delta H = 0$. This should provide a good

description of weakly interacting molecules, e.g., in solution or metal dilution experiments. However, our full model is considerably richer than a single molecule described only by the DW potential. This allows us to understand the correlation between T_{LIESST} and $T_{1/2}$ in much greater detail.

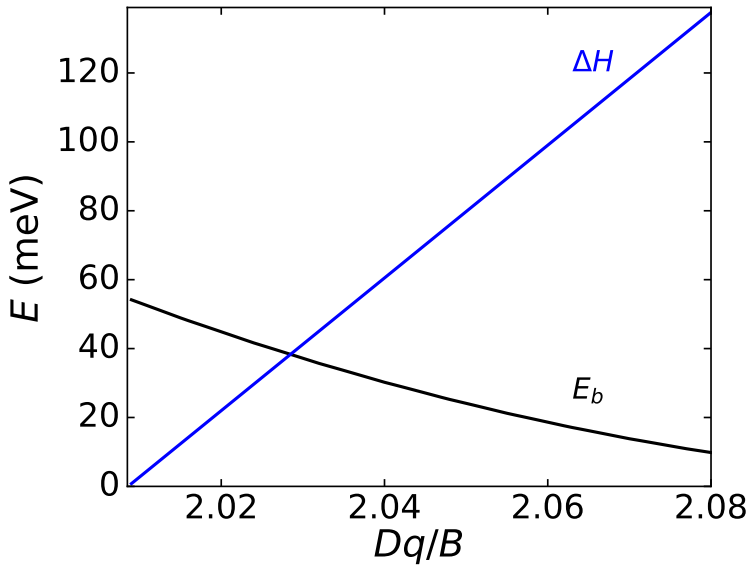

Figure S3: The effect of the crystal field strength (Dq) on the barrier height E_b and ΔH of the DW state. All other parameters have their default values, given in table 1.

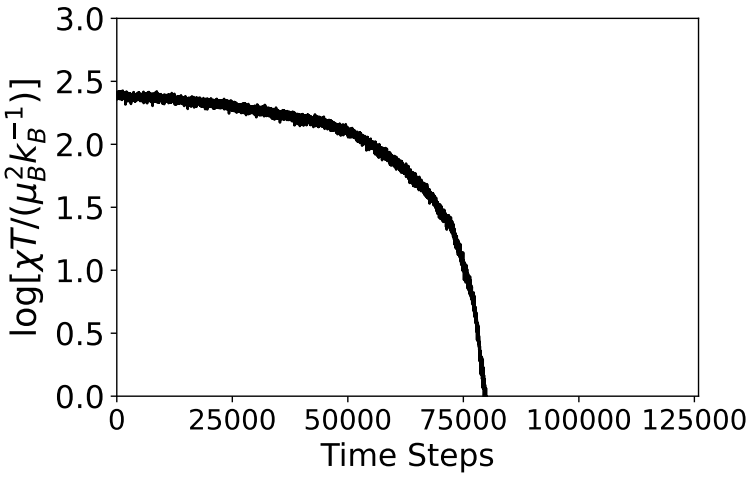

Figure S4: Non-exponential decay at $T = 60$ K. Parameters have their default values, given in table 1. For this case $T_{\mathrm{LIESST}} = 52\ K$.

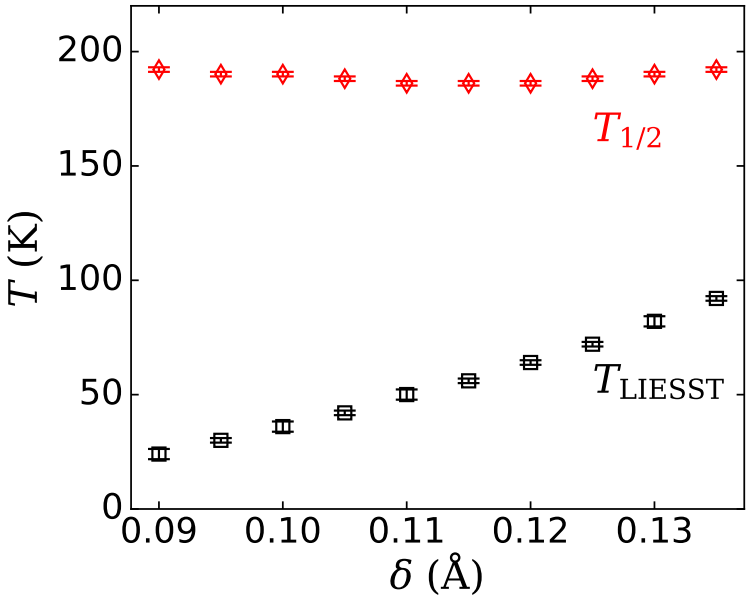

Figure S5: Influence of δ on T_{LIESST} and $T_{1/2}$. All other parameters have their default values, given in table 1.

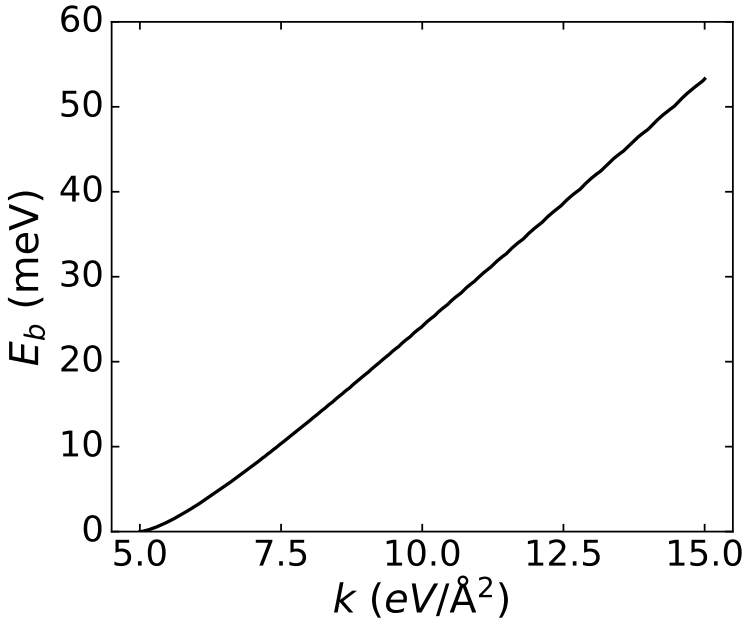

Figure S6: The effect of the inner coordination sphere stiffness, k, on the barrier height E_b. The approximately linear behavior is consistent with the prediction of equation S45 in the limit of small ΔH, which is required for SCO. All other parameters have their default values, given in table 1.

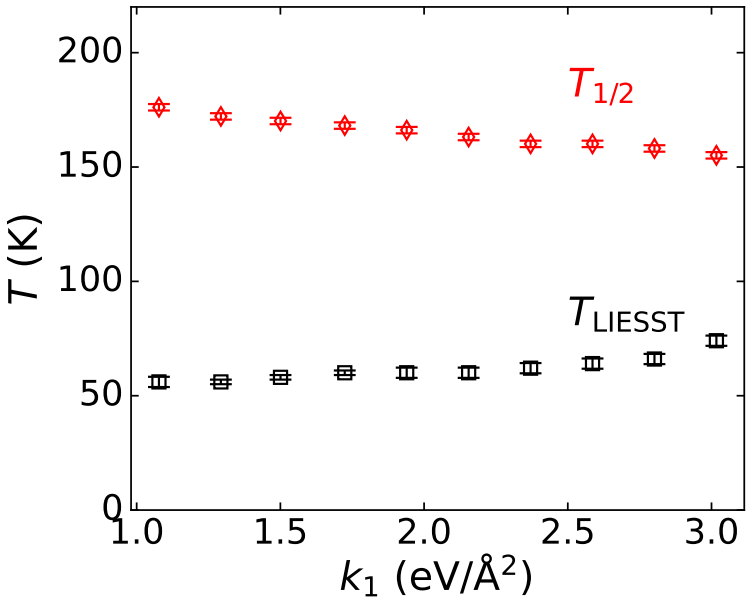

Figure S7: Influence of k_1 on T_{LIESST} and $T_{1/2}$. Here $k_2 = 0.22$ meV/Å^2 and all other parameters have their default values, given in table 1.

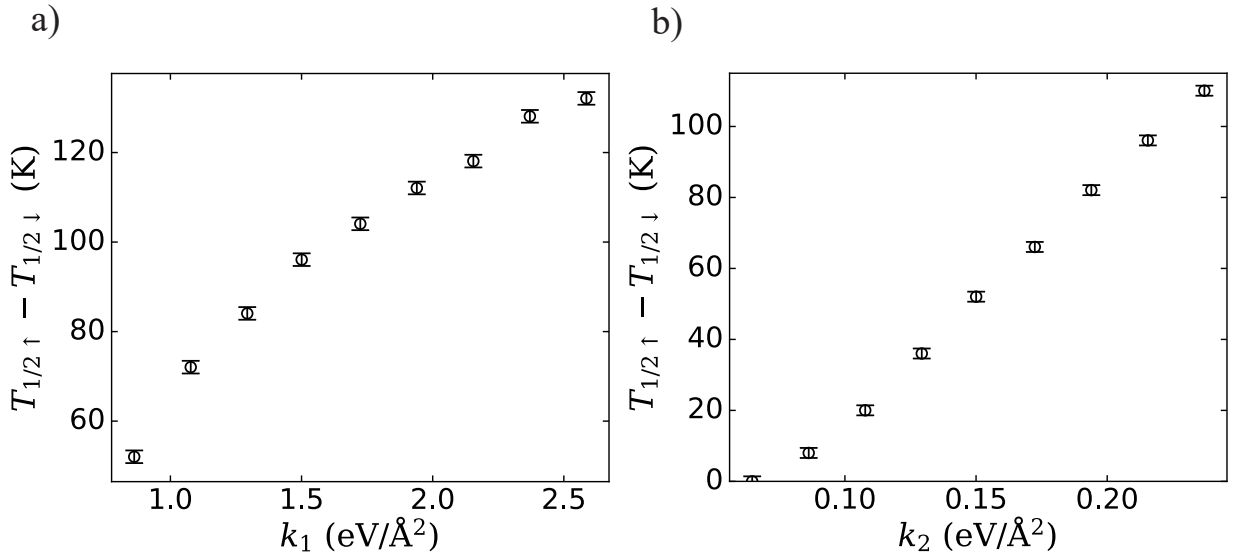

Figure S8: Hysteresis width increases with both (a) k_1 and (b) k_2. In (a) $k_2 = 0.22$ eV/Å^2. Other parameters have default the values in table 1.

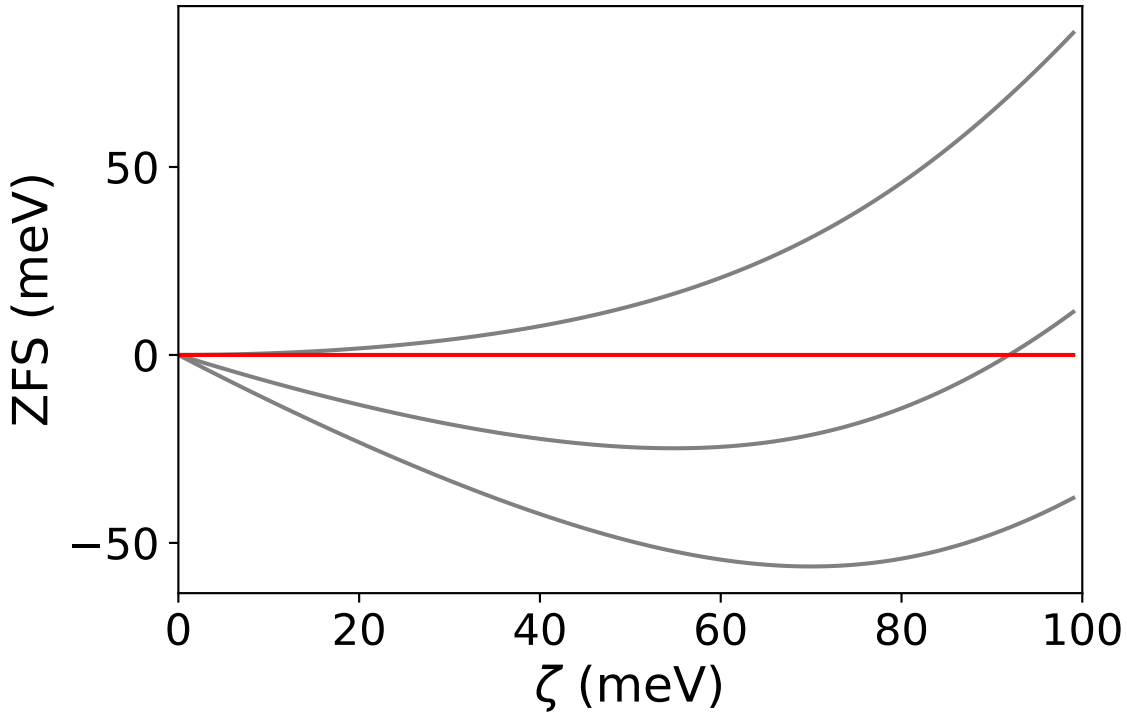

Figure S9: Spin-orbit induced zero-field splittings (ZFS) between different total angular momentum j states of the pure HS levels and the DW state at $Q = \delta$. All other parameters have their default values, given in table 1.

Table S1: Variation in the iron-ligand stretching frequencies with denticity in octahedral spin-crossover complexes. All frequencies are in cm^{-1}. Consistent with the experimental analyses of materials with different denticities we have only included mono- bi- and tridentate materials where all ligands have the same denticity. All data from infrared (IR) spectroscopy and only the symmetric mode is included where this is assigned in the cited literature. Here ptz=Pentylenetetrazol, phen=phenanthroline, pz=pyrazine, bzimpy=2,6-bis(benzimidazol-2'-yl)pyridine, tpa=Tris(2-pyridylmethyl)amine, L(II)=1-(2-pyridyl)ethyl-bis(2-pyridylmethyl)amine, and py=pyridine.

Dentictiy	**Material**	$\omega_{b,HS}$	$\omega_{b,LS}$	**Refs.**
Monodentate	$[Fe(ptz)_6](BF_6)_2$	167, 231	261/279, 412	[86,105]
Bidentate	$[Fe(CH_3O{-}phen)_3](ClO_4)_2 \cdot H_2O$	227, 237	341, 352	[86,106]
Tridentate	$[Fe(HB(pz)_3)_2]$	223, 258	400, 435, 459	[86,107]
	$[Fe(H{-}bzimpy)_2](ClO_4)_2$	220	436	[86,108]
	$[Fe(OH{-}bzimpy)_2](ClO_4)_2$	215	436	[86,108]
	$[Fe(Cl{-}bzimpy)_2](ClO_4)_2$	212	436	[86,108]
	$[Fe(CH_3{-}bzimpy)_2](ClO_4)_2$	212	436	[86,108]
	$[Fe(H{-}bzimpyH_{-1})_2]$	229	440	[86,109]
	$[Fe(OH{-}bzimpyH_{-1})_2]$	217	436	[86,109]
	$[Fe(Cl{-}bzimpyH_{-1})_2]$	213	435	[86,109]
Tetradentate	$[Fe(tpa)(NCS)_2]$	-	480	[110]
	$[FeL(II)(NCS)_2]$	-	534	[110]
Framework	$[Fe(py)_2(Pd(CN)_4)]$	217	383	[86,111]
	$[Fe(py)_2(Pt(CN)_4)]$	221	395	[86,111]
	$[Fe(pz)_2(Pt(CN)_4)]$	226	402	[111]
	$[Fe(pz)_2(Pd(CN)_4)]$	223	390	[111]
	$[Fe(pz)_2(Ni(CN)_4)]$	231	394	[111]

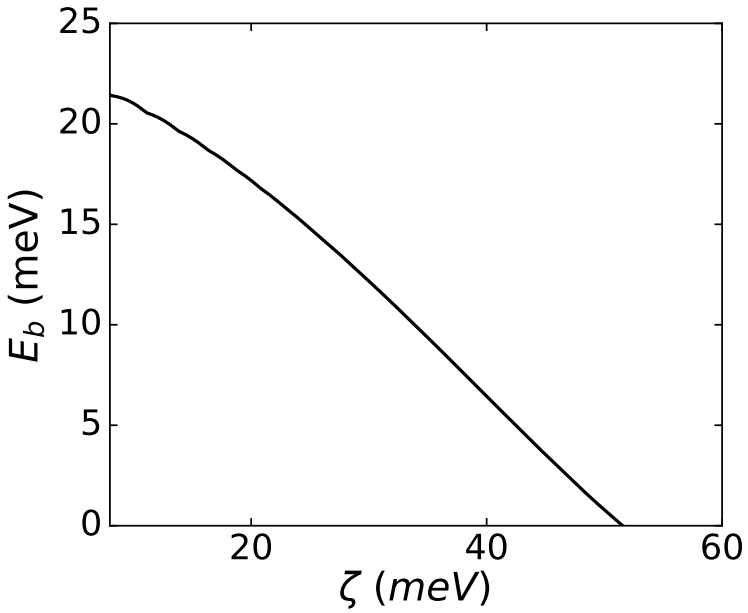

Figure S10: The effect of the spin-orbit coupling strength on the barrier height E_b. All other parameters have their default values, given in table 1.

References

(1) Vopson, M. M. The information catastrophe. *AIP Advances* **2020**, *10*, 085014.

(2) Sessoli, R.; Gatteschi, D.; Caneschi, A.; Novak, M. A. Magnetic bistability in a metal-ion cluster. *Nature* **1993**, *365*, 141–143.

(3) Tezgerevska, T.; Alley, K. G.; Boskovic, C. Valence tautomerism in metal complexes: Stimulated and reversible intramolecular electron transfer between metal centers and organic ligands. *Coord. Chem. Rev.* **2014**, *268*, 23–40.

(4) Newton, G. N.; Nihei, M.; Oshio, H. Cyanide-Bridged Molecular Squares – The Building Units of Prussian Blue. *Eur. J. Inorg. Chem.* **2011**, *2011*, 3031–3042.

(5) Catala, L.; Mallah, T. Nanoparticles of Prussian blue analogs and related coordination polymers: From information storage to biomedical applications. *Coord. Chem. Rev.* **2017**, *346*, 32.

(6) Bleuzen, A.; Marvaud, V.; Mathoniere, C.; Sieklucka, B.; Verdaguer, M. Photomagnetism in Clusters and Extended Molecule-Based Magnets. *Inorg. Chem.* **2009**, *48*, 3453–3466.

(7) Hoshino, N.; Iijima, F.; Newton, G.; Yoshida, N.; Shiga, T.; Nojiri, H.; Nakao, A.; Kumai, R.; Murakami, Y.; Oshio, H. Three-way switching in a cyanide-bridged [CoFe] chain. *Nat. Chem.* **2012**, *4*, 921.

(8) Gütlich, P.; Goodwin, H. A. *Spin crossover—an overall perspective*; Springer, 2004; pp 1–47.

(9) Khusniyarov, M. M. How to Switch Spin-Crossover Metal Complexes at Constant Room Temperature. *Chem. - Eur. J.* **2016**, *22*, 15178–15191.

(10) Bousseksou, A.; Molnár, G.; Salmon, L.; Nicolazzi, W. Molecular spin crossover phenomenon: recent achievements and prospects. *Chem. Soc. Rev.* **2011**, *40*, 3313.

(11) Garcia, Y.; Ksenofontov, V.; Gütlich, P. Spin Transition Molecular Materials: New Sensors. *Hyperfine Interactions* **2002**, *139*, 543–551.

(12) Jureschi, C. M.; Linares, J.; Rotaru, A.; Ritti, M. H.; Parlier, M.; Dîrtu, M. M.; Wolff, M.; Garcia, Y. Pressure Sensor via Optical Detection Based on a 1D Spin Transition Coordination Polymer. *Sensors* **2015**, *15*, 2388.

(13) Kahn, O.; Martinez, C. J. Spin-Transition Polymers: From Molecular Materials Toward Memory Devices. *Science* **1998**, *279*, 44–48.

(14) Kahn, O.; Kröber, J.; Jay, C. Spin Transition Molecular Materials for displays and data recording. *Adv. Mater.* **1992**, *4*, 718.

(15) Létard, J.-F.; Guionneau, P.; Goux-Capes, L. *Spin Crossover in Transition Metal Compounds III*; Springer Berlin Heidelberg: Berlin, Heidelberg, 2004; pp 221–249.

(16) Ruiz, E. Charge transport properties of spin crossover systems. *Phys. Chem. Chem. Phys.* **2014**, *16*, 14–22.

(17) Sanvito, S. Molecular spintronics. *Chem. Soc. Rev.* **2011**, *40*, 3336–3355.

(18) Cruddas, J.; Powell, B. J. Multiple Coulomb phases with temperature-tunable ice rules in pyrochlore spin-crossover materials. *Phys. Rev. B* **2021**, *104*, 024433.

(19) Manrique-Juárez, M. D.; Rat, S.; Salmon, L.; Molnár, G.; Quintero, C. M.; Nicu, L.; Shepherd, H. J.; Bousseksou, A. Switchable molecule-based materials for micro- and nanoscale actuating applications: Achievements and prospects. *Coord. Chem. Rev.* **2016**, *308*, 395–408.

(20) Mikolasek, M. et al. Complete Set of Elastic Moduli of a Spin-Crossover Solid: Spin-State Dependence and Mechanical Actuation. *J. Am. Chem. Soc.* **2018**, *140*, 8970.

(21) Muller, R. N.; Vander Elst, L.; Laurent, S. Spin Transition Molecular Materials: Intelligent Contrast Agents for Magnetic Resonance Imaging. *J. Am. Chem. Soc.* **2003**, *125*, 8405–8407, PMID: 12837114.

(22) Quintero, C. M.; Félix, G.; Suleimanov, I.; Costa, J. S.; Molnár, G.; Salmon, L.; Nicolazzi, W.; Bousseksou, A. Hybrid spin-crossover nanostructures. *Beilstein Journal of Nanotechnology* **2014**, *5*, 2230–2239.

(23) Hauser, A. *Spin Crossover in Transition Metal Compounds II*; Springer Berlin Heidelberg: Berlin, Heidelberg, 2004; pp 155–198.

(24) Chastanet, G.; Desplanches, C.; Baldé, C.; Rosa, P.; Marchivie, M.; Guionneau, P. A critical review of the T (LIESST) temperature in spin crossover materials- What it is and what it is not. *Chem. Sq* **2018**, *2*.

(25) Milin, E.; Patinec, V.; Triki, S.; Bendeif, E.-E.; Pillet, S.; Marchivie, M.; Chastanet, G.; Boukheddaden, K. Elastic Frustration Triggering Photoinduced Hidden Hysteresis and Multistability in a Two-Dimensional Photoswitchable Hofmann-Like Spin-Crossover Metal–Organic Framework. *Inorg. Chem.* **2016**, *55*, 11652–11661.

(26) Boonprab, T.; Lee, S. J.; Telfer, S. G.; Murray, K. S.; Phonsri, W.; Chastanet, G.; Collet, E.; Trzop, E.; Jameson, G. N. L.; Harding, P.; Harding, D. J. The First Observation of Hidden Hysteresis in an Iron(III) Spin-Crossover Complex. *Angew. Chem., Int. Ed.* **2019**, *58*, 11811–11815.

(27) Chakraborty, P.; Enachescu, C.; Humair, A.; Egger, L.; Delgado, T.; Tissot, A.; Guénée, L.; Besnard, C.; Bronisz, R.; Hauser, A. Light-induced spin-state switching in the mixed crystal series of the 2D coordination network [Zn1-xFex(bbtr)3](BF4)2: optical spectroscopy and cooperative effects. *Dalton Trans.* **2014**, *43*, 17786–17796.

(28) Ndiaye, M. M.; Pillet, S.; Bendeif, E.-E.; Marchivie, M.; Chastanet, G.; Boukheddaden, K.; Triki, S. Hidden Hysteretic Behavior of a Paramagnetic Iron(II) Network

Revealed by Light Irradiation. *European Journal of Inorganic Chemistry* **2018**, *2018*, 305–313.

(29) Hauser, A.; Enachescu, C.; Daku, M. L.; Vargas, A.; Amstutz, N. Low-temperature lifetimes of metastable high-spin states in spin-crossover and in low-spin iron(II) compounds: The rule and exceptions to the rule. *Coord. Chem. Rev.* **2006**, *250*, 1642–1652.

(30) Smeigh, A. L.; Creelman, M.; Mathies, R. A.; McCusker, J. K. *J. Am. Chem. Soc.* **2008**, *130*, 14105.

(31) Consani, C.; Premont-Schwarz, M.; ElNahhas, A.; Bressler, C.; van Mourik, F.; Cannizzo, A.; Chergui, M. *Angew. Chem., Int. Ed. Engl.* **2009**, *48*, 7184.

(32) Cannizzo, A.; Milne, C.; Consani, C.; Gawelda, W.; Bressler, C.; van Mourik, F.; Chergui, M. *Coord. Chem. Rev.* **2010**, *254*, 2677.

(33) Wolf, M. M. N.; Groß, R.; Schumann, C.; Wolny, J. A.; Schünemann, V.; Døssing, A.; Paulsen, H.; McGarvey, J. J.; Diller, R. *Phys. Chem. Chem. Phys.* **2008**, *10*, 4264.

(34) Lorenc, M.; Hébert, J.; Moisan, N.; Trzop, E.; Servol, M.; Buron Le-Cointe, M.; Cailleau, H.; Boillot, M. L.; Pontecorvo, E.; Wulff, M.; Koshihara, S.; Collet, E. *Phys. Rev. Lett.* **2009**, *103*, 028301.

(35) Khalil, M.; Marcus, M. A.; Smeigh, A. L.; McCusker, J. K.; Chong, H. H. W.; Schoenlein, H. W. J. *Phys. Chem. A* **2006**, *110*, 38.

(36) Gawelda, W.; Pham, V.-T.; Benfatto, M.; Zaushitsyn, Y.; Kaiser, M.; Grolimund, D.; Johnson, S. L.; Abela, R.; Hauser, A.; Bressler, C.; Chergui, M. *Phys. Rev. Lett.* **2007**, *98*, 57401.

(37) Chergui, M. *Acta Crystallogr., Sect. A* **2010**, *66*, 229.

(38) Huse, N.; Cho, H.; Hong, K.; Jamula, L.; de Groot, F. M. F.; Kim, T. K.; McCusker, J. K.; Schoenlein, R. W. *J. Phys. Chem. Lett.* **2011**, *2*, 880.

(39) Haldrup, K. et al. *J. Phys. Chem A* **2012**, *116*, 9878.

(40) Vankó, G.; Glatzel, P.; Pham, V.-T.; Abela, R.; Grolimund, D.; Borca, C. N.; Johnson, S. L.; Milne, C. J.; Bressler, C. *Angew. Chem., Int. Ed.* **2010**, *49*, 5910.

(41) Ordejón, B.; de Graaf, C.; Sousa, C. Light-Induced Excited-State Spin Trapping in Tetrazole-Based Spin Crossover Systems. *J. Am. Chem. Soc.* **2008**, *130*, 13961–13968.

(42) Pápai, M.; Vankó, G.; de Graaf, C.; Rozgonyi, T. Theoretical Investigation of the Electronic Structure of Fe(II) Complexes at Spin-State Transitions. *Journal of Chemical Theory and Computation* **2013**, *9*, 509–519, PMID: 25821416.

(43) Sousa, C.; Domingo, A.; de Graaf, C. Effect of Second-Order Spin–Orbit Coupling on the Interaction between Spin States in Spin-Crossover Systems. *Chem. - Eur. J.* **2018**, *24*, 5146–5152.

(44) Buhks, E.; Navon, G.; Bixon, M.; Jortner, J. Spin conversion processes in solutions. *J. Am. Chem. Soc.* **1980**, *102*, 2918–2923.

(45) Hauser, A. Intersystem crossing in Fe(II) coordination compounds. *Coord. Chem. Rev.* **1991**, *111*, 275–290.

(46) Hauser, A.; Vef, A.; Adler, P. Intersystem crossing dynamics in Fe(II) coordination compounds. *J. Chem. Phys.* **1991**, *95*, 8710–8717.

(47) Hauser, A. Intersystem crossing in the [Fe(ptz)6](BF4)2 spin crossover system (ptz=1-propyltetrazole). *J. Chem. Phys.* **1991**, *94*, 2741–2748.

(48) Létard, J.-F.; Chastanet, G.; Guionneau, P.; Desplanches, C. *Spin-Crossover Materials*; John Wiley & Sons, Ltd, 2013; Chapter 19, pp 475–506.

(49) Miyamachi, T.; Gruber, M.; Davesne, V.; Bowen, M.; Boukari, S.; Joly, L.; Scheurer, F.; Rogez, G.; Yamada, T. K.; Ohresser, P.; Beaurepaire, E.; Wulfhekel, W.

Robust Spin Crossover and Memristance across a Single Molecule. *Nat. Commun.* **2012**, *3*, 938.

(50) Gopakumar, T. G.; Matino, F.; Naggert, H.; Bannwarth, A.; Tuczek, F.; Berndt, R. Electron-Induced Spin Crossover of Single Molecules in a Bilayer on Gold. *Angew. Chem., Int. Ed.* **2012**, *51*, 6262.

(51) Kobke, A. et al. Reversible Coordination-Induced Spin-State Switching in Complexes on Metal Surfaces. *Nat. Nanotechnol.* **2020**, *15*, 18.

(52) Kumar, K. S.; Ruben, M. Sublimable Spin-Crossover Complexes: From Spin-State Switching to Molecular Devices. *Angew. Chem., Int. Ed.* **2019**,

(53) Kuang, G.; Zhang, Q.; Lin, T.; Pang, R.; Shi, X.; Xu, H.; Lin, N. Mechanically-Controlled Reversible Spin Crossover of Single Fe-Porphyrin Molecules. *ACS Nano* **2017**, *11*, 6295.

(54) Tong, Y.; Kelaï, M.; Bairagi, K.; Repain, V.; Lagoute, J.; Girard, Y.; Rousset, S.; Boillot, M.-L.; Mallah, T.; Enachescu, C.; Bellec, A. Voltage-Induced Bistability of Single Spin-Crossover Molecules in a Two-Dimensional Monolayer. *J. Phys. Chem. Lett.* **2021**, *12*, 11029–11034.

(55) Liu, J.; Gao, Y.; Wang, T.; Xue, Q.; Hua, M.; Wang, Y.; Huang, L.; Lin, N. Collective Spin Manipulation in Antiferroelastic Spin-Crossover Metallo-Supramolecular Chains. *ACS Nano* **2020**, *14*, 11283–11293.

(56) Murnaghan, K. D.; Carbonera, C.; Toupet, L.; Griffin, M.; Dîrtu, M. M.; Desplanches, C.; Garcia, Y.; Collet, E.; Létard, J.-F.; Morgan, G. G. Spin-State Ordering on One Sub-lattice of a Mononuclear Iron(III) Spin Crossover Complex Exhibiting LIESST and TIESST. *Chem. - Eur. J.* **2014**, *20*, 5613–5618.

(57) Garcia, Y.; Ksenofontov, V.; Mentior, S.; Dîrtu, M. M.; Gieck, C.; Bhatthacharjee, A.; Gütlich, P. Rapid Cooling Experiments and Use of an Anionic Nuclear Probe to Sense the Spin Transition of the 1D Coordination Polymers [Fe(NH2trz)3]SnF6·n H2O (NH2trz=4-amino-1,2,4-triazole). *Chem. - Eur. J.* **2008**, *14*, 3745–3758.

(58) Craig, G. A.; Sánchez Costa, J.; Roubeau, O.; Teat, S. J.; Aromí, G. Coupled Crystallographic Order–Disorder and Spin State in a Bistable Molecule: Multiple Transition Dynamics. *Chem. - Eur. J.* **2011**, *17*, 3120–3127.

(59) Gütlich, P. *Spin Crossover in Transition Metal Compounds II*; Springer Berlin Heidelberg: Berlin, Heidelberg, 2004; pp 231–260.

(60) Vankó, G.; Renz, F.; Molnár, G.; Neisius, T.; Kárpáti, S. Hard-X-ray-Induced Excited-Spin-State Trapping. *Angew. Chem., Int. Ed.* **2007**, *46*, 5306–5309.

(61) Bonhommeau, S.; Molnár, G.; Galet, A.; Zwick, A.; Real, J.-A.; McGarvey, J. J.; Bousseksou, A. One Shot Laser Pulse Induced Reversible Spin Transition in the Spin-Crossover Complex [Fe(C4H4N2)Pt(CN)4] at Room Temperature. *Angew. Chem., Int. Ed.* **2005**, *44*, 4069–4073.

(62) Létard, J.-F. Photomagnetism of iron(ii) spin crossover complexes—the T(LIESST) approach. *J. Mater. Chem.* **2006**, *16*, 2550–2559.

(63) Paradis, N.; Chastanet, G.; Palamarciuc, T.; Rosa, P.; Varret, F.; Boukheddaden, K.; Létard, J.-F. Detailed Investigation of the Interplay Between the Thermal Decay of the Low Temperature Metastable HS State and the Thermal Hysteresis of Spin-Crossover Solids. *J. Phys. Chem. C* **2015**, *119*, 20039–20050.

(64) Létard, J.-F.; Guionneau, P.; Nguyen, O.; Costa, J. S.; Marcén, S.; Chastanet, G.; Marchivie, M.; Goux-Capes, L. A Guideline to the Design of Molecular-Based Materials with Long-Lived Photomagnetic Lifetimes. *Chem. - Eur. J.* **2005**, *11*, 4582–4589.

(65) Létard, J.-F.; Capes, L.; Chastanet, G.; Moliner, N.; Létard, S.; Real, J.-A.; Kahn, O. Critical temperature of the LIESST effect in iron(II) spin crossover compounds. *Chem. Phys. Lett.* **1999**, *313*, 115–120.

(66) Kulmaczewski, R.; Trzop, E.; Kershaw Cook, L. J.; Collet, E.; Chastanet, G.; Halcrow, M. A. The role of symmetry breaking in the structural trapping of light-induced excited spin states. *Chem. Commun.* **2017**, *53*, 13268–13271.

(67) Hayami, S.; Gu, Z.-z.; Einaga, Y.; Kobayasi, Y.; Ishikawa, Y.; Yamada, Y.; Fujishima, A.; Sato, O. A Novel LIESST Iron(II) Complex Exhibiting a High Relaxation Temperature. *Inorg. Chem.* **2001**, *40*, 3240–3242.

(68) Hauser, A. Cooperative effects on the HS→ LS relaxation in the [Fe (ptz) 6](BF4) 2 spin-crossover system. *Chem. Phys. Lett.* **1992**, *192*, 65–70.

(69) Wajnflasz, J. Etude de la transition "Low Spin", "High Spin" dans les complexes octaédriques d'ion de transition. *physica status solidi (b)* **1970**, *40*, 537–545.

(70) Nishino, M.; Singh, Y.; Boukheddaden, K.; Miyashita, S. Tutorial on elastic interaction models for multistep spin-crossover transitions. *J. Appl. Phys.* **2021**, *130*, 141102.

(71) Enachescu, C.; Linarès, J.; Varret, F. Comparison of static and light-induced thermal hystereses of a spin-crossover solid, in a mean-field approach†. *J. Phys.: Condens. Matter* **2001**, *13*, 2481–2495.

(72) Boukheddaden, K.; Shteto, I.; Hôo, B.; Varret, F. m. c. Dynamical model for spin-crossover solids. I. Relaxation effects in the mean-field approach. *Phys. Rev. B* **2000**, *62*, 14796–14805.

(73) Boukheddaden, K.; Shteto, I.; Hôo, B.; Varret, F. m. c. Dynamical model for spin-crossover solids. II. Static and dynamic effects of light in the mean-field approach. *Phys. Rev. B* **2000**, *62*, 14806–14817.

(74) Paez-Espejo, M.; Sy, M.; Boukheddaden, K. Elastic Frustration Causing Two-Step and Multistep Transitions in Spin-Crossover Solids: Emergence of Complex Antiferroelastic Structures. *J. Am. Chem. Soc.* **2016**, *138*, 3202–3210, PMID: 26860531.

(75) Cruddas, J.; Powell, B. J. Spin-State Ice in Elastically Frustrated Spin-Crossover Materials. *J. Am. Chem. Soc.* **2019**, *141*, 19790–19799, PMID: 31714072.

(76) Cruddas, J.; Powell, B. J. Structure–property relationships and the mechanisms of multistep transitions in spin crossover materials and frameworks. *Inorg. Chem. Front.* **2020**, *7*, 4424–4437.

(77) Cruddas, J.; Ruzzi, G.; Powell, B. J. Spin-state smectics in spin crossover materials. *J. Appl. Phys.* **2021**, *129*, 185102.

(78) Sugano, S. *Multiplets of Transition-Metal Ions in Crystals*; Elsevier Science, 2012.

(79) Griffith, J. S. *The theory of transition-metal ions*; Cambridge University Press, 1964.

(80) Hauser, A. Ligand field theoretical considerations. *Spin Crossover in Transition Metal Compounds I* **2004**, 49–58.

(81) Dunn, T. M. Spin-orbit coupling in the first and second transition series. *Trans. Faraday Soc.* **1961**, *57*, 1441–1444.

(82) Neese, F.; Solomon, E. I. Calculation of Zero-Field Splittings, g-Values, and the Relativistic Nephelauxetic Effect in Transition Metal Complexes. Application to High-Spin Ferric Complexes. *Inorg. Chem.* **1998**, *37*, 6568–6582.

(83) Kondo, M.; Yoshizawa, K. A theoretical study of spin–orbit coupling in an Fe (II) spin-crossover complex. Mechanism of the LIESST effect. *Chem. Phys. Lett.* **2003**, *372*, 519–523.

(84) D'Avino, G.; Painelli, A.; Boukheddaden, K. Vibronic model for spin crossover complexes. *Phys. Rev. B* **2011**, *84*, 104119.

(85) Jung, J.; Spiering, H.; Yu, Z.; Gütlich, P. The debye-waller factor in spincrossover molecular crystals: a mössbauer study on $[Fe_xZn_{1-x}(ptz)_6](BF_4)_2$. *Hyperfine Interactions* **1995**, *95*, 107–128.

(86) Tuchagues, J.-P.; Bousseksou, A.; Molnár, G.; McGarvey, J. J.; Varret, F. *Spin Crossover in Transition Metal Compounds III*; Springer Berlin Heidelberg: Berlin, Heidelberg, 2004; pp 84–103.

(87) Paulsen, H.; Trautwein, A. X. *Spin Crossover in Transition Metal Compounds III*; Springer Berlin Heidelberg: Berlin, Heidelberg, 2004; pp 197–219.

(88) Cecconi, F.; Di Vaira, M.; Midollini, S.; Orlandini, A.; Sacconi, L. Singlet .dblharw. quintet spin transitions of iron(II) complexes with a P4Cl2 donor set. X-ray structures of the compound FeCl2(Ph2PCH:CHPPh2)2 and of its acetone solvate at 130 and 295 K. *Inorg. Chem.* **1981**, *20*, 3423–3430.

(89) Ruzzi, G.; Cruddas, J.; McKenzie, R. H.; Powell, B. J. Hidden Devil's staircase in a two-dimensional elastic model of spin crossover materials. 2021.

(90) Ye, H.-Z.; Sun, C.; Jiang, H. Monte-Carlo simulations of spin-crossover phenomena based on a vibronic Ising-like model with realistic parameters. *Phys. Chem. Chem. Phys.* **2015**, *17*, 6801–6808.

(91) Khosla, A. L.; Jacko, A. C.; Merino, J.; Powell, B. J. Spin-orbit coupling and strong electronic correlations in cyclic molecules. *Phys. Rev. B* **2017**, *95*, 115109.

(92) Powell, B. J.; Merino, J.; Khosla, A. L.; Jacko, A. C. Heisenberg and Dzyaloshinskii-Moriya interactions controlled by molecular packing in trinuclear organometallic clusters. *Phys. Rev. B* **2017**, *95*, 094432.

(93) Powell, B. J.; Kenny, E. P.; Merino, J. Dynamical Reduction of the Dimensionality

of Exchange Interactions and the "Spin-Liquid" Phase of κ-(BEDT$-$TTF)$_2X$. *Phys. Rev. Lett.* **2017**, *119*, 087204.

(94) Nosé, S. A unified formulation of the constant temperature molecular dynamics methods. *J. Chem. Phys.* **1984**, *81*, 511–519.

(95) Nosé, S. An extension of the canonical ensemble molecular dynamics method. *Molecular Physics* **1986**, *57*, 187–191.

(96) Rapaport, D.; Rapaport, D. *The Art of Molecular Dynamics Simulation*; Cambridge University Press, 2004.

(97) Sciortino, N. F.; Scherl-Gruenwald, K. R.; Chastanet, G.; Halder, G. J.; Chapman, K. W.; Létard, J.-F.; Kepert, C. J. Hysteretic Three-Step Spin Crossover in a Thermo- and Photochromic 3D Pillared Hofmann-type Metal–Organic Framework. *Angewandte Chemie International Edition* **2012**, *51*, 10154–10158.

(98) Ashcroft, N. Solid state physics [by] Neil W. Ashcroft [and] N. David Mermin. 1976.

(99) Bousseksou, A.; McGarvey, J. J.; Varret, F.; Real, J. A.; Tuchagues, J.-P.; Dennis, A. C.; Boillot, M. L. Raman spectroscopy of the high- and low-spin states of the spin crossover complex Fe(phen)2(NCS)2: an initial approach to estimation of vibrational contributions to the associated entropy change. *Chem. Phys. Lett.* **2000**, *318*, 409–416.

(100) Nishino, M.; Boukheddaden, K.; Miyashita, S. Molecular dynamics study of thermal expansion and compression in spin-crossover solids using a microscopic model of elastic interactions. *Phys. Rev. B* **2009**, *79*, 012409.

(101) Turner, J. W.; Schultz, F. A. Coupled electron-transfer and spin-exchange reactions. *Coord. Chem. Rev.* **2001**, *219-221*, 81–97.

(102) Ohlrich, M.; Powell, B. J. Fast, accurate enthalpy differences in spin crossover crystals from DFT+U. *J. Chem. Phys.* **2020**, *153*, 104107.

(103) Ronayne, K. L.; Paulsen, H.; Höfer, A.; Dennis, A. C.; Wolny, J. A.; Chumakov, A. I.; Schünemann, V.; Winkler, H.; Spiering, H.; Bousseksou, A.; Gütlich, P.; Trautwein, A. X.; McGarvey, J. J. Vibrational spectrum of the spin crossover complex [Fe(phen)2(NCS)2] studied by IR and Raman spectroscopy, nuclear inelastic scattering and DFT calculations. *Phys. Chem. Chem. Phys.* **2006**, *8*, 4685–4693.

(104) Marcus, R. A. Electron transfer reactions in chemistry. Theory and experiment. *Rev. Mod. Phys.* **1993**, *65*, 599–610.

(105) Mueller, E. W.; Ensling, J.; Spiering, H.; Guetlich, P. High-spin .dblharw. low-spin transition in hexacoordinate complexes of iron(II) with monodentate 1-alkyltetrazole ligands: a variable-temperature Moessbauer, magnetic susceptibility, and far-infrared study. *Inorg. Chem.* **1983**, *22*, 2074–2078.

(106) Fleisch, J.; Guetlich, P.; Hasselbach, K. M.; Mueller, W. New aspects of the high spin-low spin transition in tris(2-methyl-1,10-phenanthroline)iron(II) perchlorate. *Inorg. Chem.* **1976**, *15*, 958–961.

(107) Grandjean, F.; Long, G. J.; Hutchinson, B. B.; Ohlhausen, L.; Neill, P.; Holcomb, J. D. Study of the high-temperature spin-state crossover in the iron(II) pyrazolylborate complex Fe[HB(pz)3]2. *Inorg. Chem.* **1989**, *28*, 4406–4414.

(108) Enamullah, M.; Linert, W.; Gutmann, V. Vibrational spectroscopy on iron(II) spin-crossover complexes with 4-substituted 2,6-bis(benzimidazol-2'-yl)pyridine. *Vibrational Spectroscopy* **1995**, *9*, 265–271.

(109) Enamullah, M.; Renz, F.; El-Ayaan, U.; Wiesinger, G.; Linert, W. Experimental spin-crossover investigations on charged and neutral iron(II) complexes with 4-substituted-2,6-bis-(benzimidazol-2'-yl)pyridine. *Vibrational Spectroscopy* **1997**, *14*, 95–104.

(110) Højland, F.; Toftlund, H.; Yde-Andersen, S. Spin Equilibria in Some New cis-Diisothiocyanato Iron(II) Complexes with Tetradentate Ligands of the Tris(2-pyridylmethyl)amine Type. *Acta Chem. Scand. A* **1983**, *37*, 251–257.

(111) Molnár, G.; Niel, V.; Gaspar, A. B.; Real, J.-A.; Zwick, A.; Bousseksou, A.; McGarvey, J. J. Vibrational Spectroscopy of Cyanide-Bridged, Iron(II) Spin-Crossover Coordination Polymers: Estimation of Vibrational Contributions to the Entropy Change Associated with the Spin Transition. *J. Phys. Chem. B* **2002**, *106*, 9701–9707.